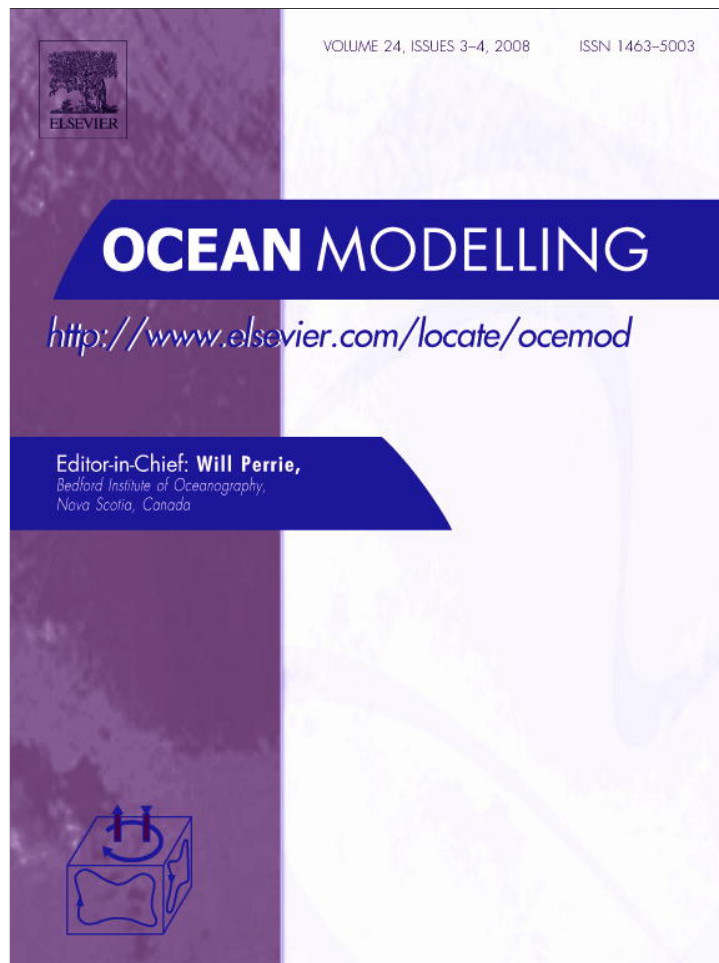


Provided for non-commercial research and education use.
Not for reproduction, distribution or commercial use.



This article appeared in a journal published by Elsevier. The attached copy is furnished to the author for internal non-commercial research and education use, including for instruction at the authors institution and sharing with colleagues.

Other uses, including reproduction and distribution, or selling or licensing copies, or posting to personal, institutional or third party websites are prohibited.

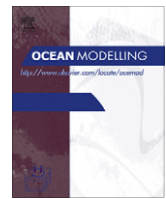
In most cases authors are permitted to post their version of the article (e.g. in Word or Tex form) to their personal website or institutional repository. Authors requiring further information regarding Elsevier's archiving and manuscript policies are encouraged to visit:

<http://www.elsevier.com/copyright>



Contents lists available at ScienceDirect

Ocean Modelling

journal homepage: www.elsevier.com/locate/ocemod

Performance of two-equation turbulence closures in three-dimensional simulations of the Red Sea overflow

Mehmet Ilıcak^{a,*}, Tamay M. Özgökmen^a, Hartmut Peters^a, Helmut Z. Baumert^b, Mohamed Iskandarani^a

^aRosenstiel School of Marine and Atmospheric Science, Meteorology and Physical Oceanography, 4600 Rickenbacker Causeway, MPO/RSMAS, Miami, FL 33149, USA

^bFreie Universität, Dept. Mathematik and Computer Science, Berlin, Germany

ARTICLE INFO

Article history:

Received 6 February 2008

Received in revised form 30 May 2008

Accepted 2 June 2008

Available online 13 June 2008

Keywords:

Red Sea overflow

$k-\varepsilon$

$k-\omega$

Two-equation turbulence model

Mixing

ABSTRACT

Mixing of overflows released from polar and marginal seas is a key process shaping the structure of the meridional overturning circulation. Ocean general circulation models have difficulty in resolving the overflows, and therefore they must rely on parameterizations. In this study, the performance of a set of turbulence closures in reproducing mixing of an overflow is quantified. We simulate the Red Sea overflow by employing standard $k-\varepsilon$, $k-\omega$ and Mellor–Yamada schemes with various stability functions, as well as a modified $k-\varepsilon$ model that relies on the prescription of the turbulent Prandtl number rather than on stability functions. The simpler KPP mixing scheme and experiments without turbulent fluxes serve as useful references. To our knowledge, this is the first time that the performance of two-equation turbulence models has been examined so closely using data from an overflow.

It is found that without turbulence closures, the hydrodynamic model has difficulty in reproducing the correct three-dimensional pathway of the Red Sea overflow, consisting of a distinct bifurcation into two diverging channels. All turbulence models capture the vertical structure of this overflow consisting of an interfacial layer, characterized by the density gradient, and a well-mixed bottom layer. Mean eddy diffusivity values from most closures are comparable those from observations. But we find that KPP leads to eddy diffusivity values that are too small while those from Mellor–Yamada with Galperin [Galperin, B., Kantha, L.H., Hassid, S., Rosati, A., 1988. A quasi-equilibrium turbulent energy model for geophysical flows. *J. Atmos. Sci.* 45, 55–62] stability functions are too large. Such high diffusivities lead to excessive mixing in the bottom layer of the overflow, ultimately resulting in a salinity deficit of approximately 1 psu in the product water mass. Salinity deviations between the models and observations are quantified using both data taken along the channels and two sections across the overflow. KPP and Mellor–Yamada with Galperin (1988) stability functions produce the largest deviations from the observations, while the modified $k-\varepsilon$ exhibits the smallest deviations. The other four closures fall in between, showing results similar to one another. The performance of the Mellor–Yamada turbulence closure is improved considerably by using the stability functions by Kantha and Clayson [Kantha, L.H., Clayson, C.A., 1994. An improved mixed layer model for geophysical applications. *J. Geophys. Res.* 99 (December), 25235–25266], which allow for a stationary Richardson number of 0.21. In conclusion, we find that most turbulence closures lead to a satisfactory reproduction of the Red Sea overflow, within the temporal and spatial sampling uncertainties of the REDSOX data, provided that fairly high-resolution regional models are used.

© 2008 Elsevier Ltd. All rights reserved.

1. Introduction

The transport and properties (i.e. temperature and salinity) of the deep and intermediate water masses are important for the meridional overturning circulation (MOC). Understanding the physics behind the MOC is important since it relates to the role of ocean in climate dynamics. Most of the deep and intermediate water masses are transported to depth and modified in overflows from polar seas by cooling (e.g., Dickson et al., 1990) and from mar-

ginal seas by evaporation (e.g., Baringer and Price, 1997; Bower et al., 2005). The overflows change the properties of the source water, bottom water in polar seas and marginal seas, by entrainment and mixing into the properties of the product water which is released into the general circulation (Price and Baringer, 1994). Such modification occurs at much smaller temporal and spatial scales than the large-scale MOC. Therefore, the representation of overflows in general ocean circulation models is a challenge. Since overflows are important, they have been studied extensively, e.g., Girton et al. (2001) for the Denmark Strait overflow, Gordon et al. (2004) for Antarctic shelves overflows, Baringer and Price (1997) for the Mediterranean Sea overflow, and (Peters et al., 2005a) for the Red Sea

* Corresponding author. Tel.: +1 7863251094.

E-mail address: milicak@rsmas.miami.edu (M. Ilıcak).

overflow. One of the primary findings common to all these studies is that not only the properties of the source water but also the small-scale mixing in the overflows and their ambient stratification determine the product water properties.

Shear instabilities associated with stably-stratified flows (e.g. Kelvin–Helmholtz vortices) are one of the key turbulent coherent structures responsible for mixing in overflows. These vertical eddies occur on small-scales in time and space ($O(\text{min})$ in time and $O(\text{m})$ in spatial). The small-scale nature of the gravity currents prevents their explicit resolution in ocean general circulation models (OGCMs) used in climate models (Wu et al., 2007). Furthermore, most of the ocean general circulation models employ the hydrostatic approximation, and therefore they can not capture the overturning eddies. Thus, OGCMs must rely entirely on the accuracy of vertical mixing schemes or parameterizations.

Development of a mixing parameterization relies on two fundamental steps. The first is the existence of truth or benchmarks that provide the physical metrics necessary to validate the parameterizations. The second is the theoretical model determining the form of the parameterization.

There are three different avenues that provide benchmarks for parameterizations of overflow mixing. The first is to conduct laboratory experiments (e.g., Ellison and Turner, 1959; Hallworth et al., 1996; Baines, 2001; Cenedese et al., 2004). Their main advantage is that large ensembles of experiments can be performed with known parameters and real fluid. There are two main drawbacks of laboratory experiments. The first is that the Reynolds number, the ratio of inertial to viscous forces, is orders of magnitude smaller in laboratory experiments than in the ocean. Second, there are some technical difficulties associated with experiments of bottom gravity current. For instance, the topographic slopes used in the laboratory are much steeper than those encountered in nature. Overflows propagate over gentle slopes in the real ocean (less than 1°), whereas fluids cannot achieve enough speed with such gentle slopes within the confines of a laboratory tank, on the $O(10\text{ m})$. Simply put, one cannot fit a real overflow into a laboratory tank. Nevertheless, laboratory experiments are extremely useful to understand the some of the principal physics of bottom gravity currents (Simpson, 1987). They have been also used to develop simple mixing parameterizations in early models of overflows (Killworth, 1977).

The second approach to validate parameterization of overflow mixing comes with recent improvement of the computational power. High resolution nonhydrostatic numerical models can be used to develop and validate parameterizations. Idealized bottom gravity currents have been simulated using high-resolution nonhydrostatic models in 2D and 3D settings over smooth topography (Özgökmen and Chassignet, 2002; Özgökmen et al., 2004a), over complex geometry (Özgökmen et al., 2004b), in the presence of ambient stratification (Özgökmen et al., 2006) and to explore the combined effect of complex topography and ambient stratification (Özgökmen and Fischer, 2008). The main advantage of this approach is the flexibilities in setting domain geometry and parameter space. Also, all simulations have exact numbers associated with them, as opposed to measuring errors encountered elsewhere. The disadvantages include the fact that the fluid is not real and not all degrees of freedom of turbulent flow interactions are resolved. For instance, all the above-mentioned studies can be classified as large eddy simulations, in which the energy-containing turbulent flow structures are resolved in time and space, and the effect of smaller eddies on the resolved fields is parameterized through sub-grid scale models. Furthermore, even on parallel machines, such numerical experiments take much longer than reality, typically by an order of magnitude. Both laboratory and numerical experiments permit a systematic exploration of a controlled ensemble of realizations that are particularly suited to study a problem.

The third approach is to use real ocean observations as benchmarks for validation of mixing parameterizations. This approach has been followed by Jungclaus and Mellor (2000) and Xu et al. (2006) using data from the Mediterranean outflow. Ilıcak et al. (2008) and Chang et al. (2008) relied on observational data from the Red Sea overflow to test mixing parameterizations in 2D and 3D hydrodynamic models, respectively. The main advantage of this avenue is that oceanic overflows pose the ultimate tests for this problem and this approach aims directly at the target. But the disadvantage is that in many cases the data is not synoptic, namely the temporal gap between the observations is longer than it takes for the overflow to change (e.g. $O(1\text{ day})$), while the spatial sampling can also be insufficient to capture critical locations that can cause mixing.

The second fundamental component of parameterization development, namely mathematical models of turbulent mixing, can be broadly separated into two groups; the first group consists of simple algebraic models that are used to evaluate the eddy diffusivity and eddy viscosity. The biggest advantage of these models is that they are computationally inexpensive. The frequently used K-profile parameterization (KPP, Large et al., 1994; Large and Gent, 1999) is an example of a diagnostic model. In KPP, the vertical viscosity is specified as a dimensional constant times a simple function of the gradient Richardson number, $Ri = N^2 / [(\partial v / \partial z)^2 + (\partial u / \partial z)^2]$. Another diagnostic model is the Turner parameterization (TP) developed by Hallberg (2000) to prescribe the entrainment velocity as a simple function of the bulk Richardson number. The dynamics behind TP is based on the laboratory study by Ellison and Turner (1959) and Turner (1986). It was further modified by Chang et al. (2005) who used an isopycnic model in an idealized gravity current problem and compared its performance with that of a 3D nonhydrostatic model. Xu et al. (2006) further improved this approach to simulate the Mediterranean overflow. Chang et al. (2008) employed the same modified version of TP as well as KPP to simulate the Red Sea overflow. The main disadvantage of these models is that they are physically simple. For instance, the concept of Ri being the main controlling parameter for mixing arises from the assumption that there is a steady-state and local balance between shear and buoyancy production. As such, we are motivated to pursue other, more complex models in which this assumption is not made.

The second group of parameterizations consists of so-called two-equation or second-order turbulence closures. The governing equations are based on the Reynolds-averaged Navier–Stokes (RANS) equations, in which field variables are separated into mean and turbulent components. In addition to the mean flow equations, one or more differential equations are integrated in time to calculate eddy viscosity and diffusivity in these models. Unknowns are the turbulent kinetic energy, k , and some combination of turbulent length scale, l , dissipation rate, ϵ , and turbulent frequency, ω . Two-equation turbulent closure models have been used extensively in oceanographic applications (Rodi, 1980; Mellor and Yamada, 1982; Kantha and Clayson, 1994; Burchard and Baumert, 1995; Baumert and Peters, 2000; Canuto et al., 2001; Baumert and Peters, 2004; Umlauf and Burchard, 2005; Peters and Baumert, 2007). The two-equation Mellor–Yamada model (Mellor and Yamada, 1982) has been used in overflow studies by Jungclaus and Mellor (2000), Ezer and Mellor (2004) and Ezer (2005). Additionally, Ezer (2006) used a high-resolution hydrostatic model with Mellor–Yamada turbulence closure to simulate an idealized Faroe Bank Channel overflow, and compared model results with the field observations of Mauritzen et al. (2005) and Geyer et al. (2006). Burchard et al. (2005) employ $k-\epsilon$ turbulence closure to simulate 3D idealized case of medium-intensity dense water plumes in the Arkona Basin. Arneborg et al. (2007) employ a 1D $k-\omega$ turbulence closure to understand the dynamics of a gravity current in

the Baltic Sea. They compare the model results with microstructure observations. Recently, Burchard et al. (2008) quantify the mixing of the gravity current in the Western Baltic Sea using k - ϵ turbulence closure.

The main objective of the present study is to compare different two-equation turbulence closures in 3D numerical simulations of the Red Sea overflow. Four turbulence closure models are selected for the comparison. Three of them, k - ϵ , k - ω , and MY2.5, are the turbulence closures with complex stability functions representing the effects of buoyancy and shear. The fourth scheme is the modified k - ϵ turbulence closure of Peters and Baumert (2007). In their model, a simple gradient Richardson number-dependent turbulent Prandtl number is used instead of complex stability functions. Peters and Baumert (2007) validate this modified closure by comparing it with microstructure observations from a stratified and sheared tidal estuary and with laboratory experiments. We also employ KPP since it is a widely used diagnostic parameterization in climate models. We further performed a control experiment in which both vertical eddy viscosity and eddy diffusivity were set to zero in an effort to understand the performance of the turbulence schemes. The accuracy of the model results is evaluated using hydrographic and current observations collected in the Red Sea outflow experiments (Peters et al., 2005b; Peters and Johns, 2005; Bower et al., 2005).

Results indicate that all turbulence closures show a reasonable agreement with observational data except that with MY2.5 with Galperin stability functions bottom salinities are too low by 1 psu. The control experiment exhibits poor performance in that the characteristic bifurcation of the overflow into two distinct channels cannot be reproduced and the overflow characteristics are therefore significantly different compared to the others.

This paper is organized as follows: The main characteristics of the Red Sea overflow from the observational experiments conducted in 2001 are summarized in Section 2. The numerical model and turbulence closures are then introduced in Section 3, and the evaluation strategy and setup of numerical experiments are described in Section 4. The main results are presented in Section 5. Finally we summarize and conclude in Section 6.

2. Character and dynamics of the Red Sea outflow

The main characteristics of the Red Sea overflow water (RSOW) are summarized in the following. The Red Sea region is hot and dry with high evaporation of about 2 m/yr (Bower et al., 2002). The dense Red Sea water is formed at its northern end in winter (Sofianos and Johns, 2001). This dense, warm and salty water leaves the Red Sea through the 150 km long and comparatively narrow strait of Bab el Mandeb (BAM) which has a sill depth of 150 m (Murray and Johns, 1997). South of Bab el Mandeb the outflow divides into two channels, a northern channel (NC) typically 5 km wide and 130 km long paralleling the Yemeni coast, and a wider and shallower southern channel (SC) toward the Djibouti coast (Peters et al., 2005b). These channels end at about 800 m depth at the drop-off into 1600 m deep Tadjura Rift as shown in Fig. 1.

The Red Sea outflow experiment (REDSOX) of 2001 is the first comprehensive study of the RSOW, south of Bab el Mandeb Strait throughout Gulf of Aden, where RSOW equilibrates and spreads into the ambient water. REDSOX was a joint program between Rosenstiel School of Marine and Atmospheric Science and the Woods Hole Oceanographic Institution. It was designed to understand the structure, dynamics and mixing of the Red Sea overflow. Two cruises were performed in 2001, one in the winter (REDSOX-1) when the outflow is maximum and one in the summer (REDSOX-2) when the outflow is minimum. The observations have three components: (i) 108 conductivity-temperature-depth (CTD) and lowered Acoustic Doppler Current Profilers (LADCP) describe the three dimensional water property distributions and circulation characteristics between BAM and the Tadjura Rift. (ii) Direct measurements of turbulent mixing were made to study the bottom stress in descending plumes. (iii) Acoustically tracked drifters were launched to study the spreading of the RSOW in the entire Gulf of Aden. The reader is referred to Bower et al. (2002), Peters and Johns (2005), Bower et al. (2005), Peters and Johns (2006), Peters et al. (2005b) and Matt and Johns (2007) for the complete analysis of the observational results.

One of the major developments during this program concerns the vertical structure of the Red Sea overflow. Peters et al.

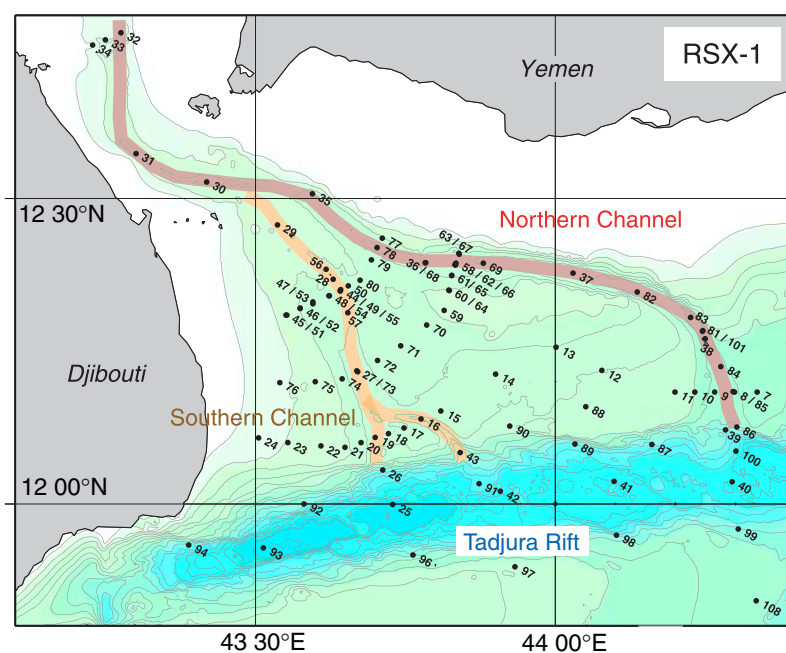


Fig. 1. Sea floor topography in the Red Sea outflow area in the western Gulf of Aden. Depth is contoured every 100 m. The Northern and Southern channels are highlighted. Numbers indicate CTD/LADCP stations from the REDSOX 2001.

(2005b) defined two distinct layers to describe the vertical structure of the overflow, the bottom layer (BL), and the interfacial layer (IL). The former reaches from the bottom to a height where the velocity is maximum, and the latter extends from this maximum upward with strong stratification and large shear. The BL is well-mixed and maintains high salinities along the northern channel. The ratio of stratification to shear leads to low Richardson numbers in both the IL and BL. While the water in the BL remains relatively undiluted along the length of the northern channel, the IL shows strong mixing and dilution of RSOW. Entrainment of ambient waters thus mainly affects the IL. It is noteworthy that the IL carries more than half of the vertically integrated volume transport near the lower end of the northern channel. The distinct vertical structure and properties of BL and IL determine the vertical distribution of density, temperature and salinity of the product waters. Therefore, if a model is to faithfully reproduce the overflow characteristics, it has to capture its vertical structure consisting of BL and IL.

3. The numerical model

3.1. Model configuration

The regional ocean modeling system (ROMS) was chosen in this study mainly because ROMS has the generic length scale scheme of Umlauf and Burchard (2003) which allows us to easily test different two-equation turbulence closures. ROMS is a free-surface, hydrostatic, primitive equations ocean model that uses orthogonal curvilinear horizontal coordinates on an Arakawa C grid. The primitive equations are discretized over topography in the vertical using stretched terrain-following, or “sigma”, coordinates (Song and Haidvogel, 1994; Shchepetkin and McWilliams, 2005).

The computational domain covers the area between the longitudes 43°E and 46°E, and latitudes 11.7°N and 13°N (Fig. 2). The sea floor topography is crucial for the model configuration because of the narrow channels which constrain the flow of the gravity currents. A detailed discussion of the topography can be found in

Chang et al. (2008), who used the same topography as herein. The topography is based on multi-beam echosoundings taken during REDSOX and a cruise of the French R/V L'Atalante (Hébert et al., 2001). These measurements have a resolution of approximately 30 m. Far field areas and gaps were filled from the 2' grid sea floor data of Smith and Sandwell (1997). The east and the south sides of the domain are extended to use open boundary conditions effectively. The north and the west boundaries are closed. A nonuniform grid is used in the model with 250 m resolution around the channels and the bifurcation point where the two channels separate at approximately 43.5°E and 12.5°N (Fig. 2). The resolution gradually coarsens to 3 km toward the end of the domain in all experiments. In the vertical, 30 sigma layers are used. With the help of a logarithmic distribution, most of the layers are placed near the bottom. All experiments are performed with $320 \times 180 \times 30$ grid points in x, y, and z directions, respectively. (Fig. 2). The baroclinic time step is set to 40 s, and 20 barotropic time steps are used between each baroclinic time step. Pressure-gradient error is a well-known problem in terrain-following models. To minimize this error, bathymetry is smoothed so that Beckmann-Haidvogel (Beckmann and Haidvogel, 1993) criterion is satisfied. We also use parabolic splines density Jacobian method (Shchepetkin and McWilliams, 2003) to calculate pressure-gradient forces. Vertical advection equation for tracer is discretized by 4th order center difference scheme. A test case was run with a stable stratification and closed boundaries which should not produce any velocities. Erroneous speeds were less than 0.01 m s^{-1} , and they were generated only in the Tadjura Rift outside the channels, where our study was focused. Since baroclinic velocities of $0.4\text{--}0.6 \text{ m s}^{-1}$ are to be expected around that area, these errors are acceptable.

Temperature (T) and salinity (S) profiles from a REDSOX station denoted T1 in Fig. 2, located near the deepest part of the Tadjura Rift and outside of the overflows pathways, are used as an initial condition for the stratification in the model domain setup. Station T1 is selected since it is as deep or deeper than the entire domain, and it is the least affected from the overflows in the Tadjura Rift. The profile from this location is cropped to the local water depth

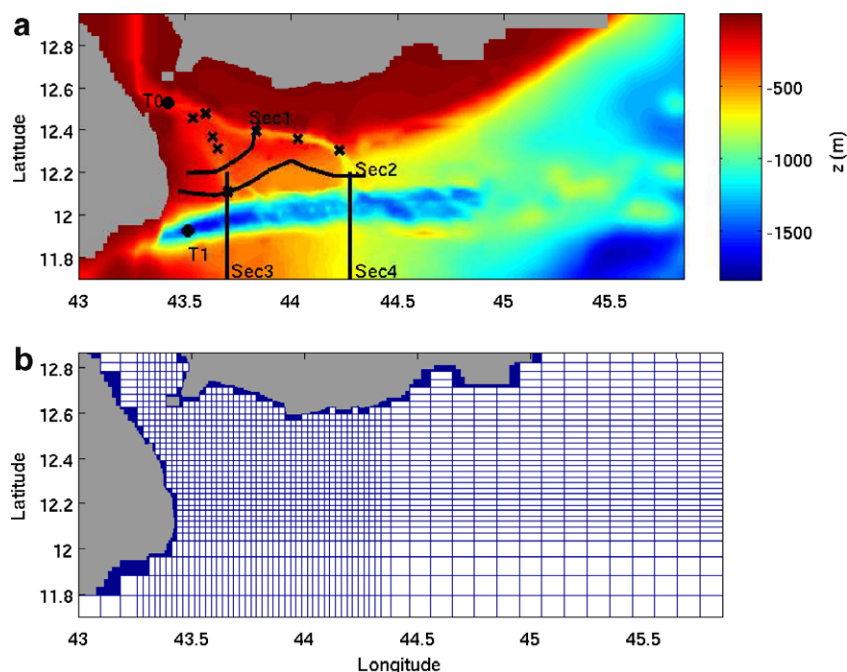


Fig. 2. (a) Model domain and bottom topography. Crosses represent the stations selected for the model comparisons. Two sections across the outflow, Sections 1 and 2, are also used to compare models results to those from the REDSOX-1 cruise. (b) Model grid plotted at every fifth point.

at any other location. Dense overflow water is introduced into the domain as follows. At the north-western side of the domain, dense water which represents the overflow coming from Bab el Mandeb Strait is released. T - S profiles in this area are relaxed towards profiles taken from the REDSOX observations in the Bab el Mandeb Strait. We further ensure that downstream of the relaxation zone simulated T - S and velocity profiles show a good agreement with the observations at REDSOX-1 station 30 (T_0 in the Fig. 2). This station serves as a checkpoint to confirm the realism of the overflow source water T - S properties and the velocity distributions.

A nonlinear equation of state (Jackett and McDougall, 1995) is used along with open boundary conditions (Marchesiello et al., 2001) at the south and east boundaries. Once the dense water is released from the top of the domain, the model is integrated for 34 days. This integration time is chosen for the overflow to reach a quasi-steady state along the channels since we know from the observations that most of the mixing occurs in the northern and southern channel. Wind forcing as well as evaporation, precipitation and radiative heat fluxes are set to zero everywhere. We have thus simplified the regional atmospheric forcing such as to be represented exclusively through the overflow source properties. Bottom drag coefficients from overflow observations indicate a wide range of $1 \times 10^{-3} \leq C_d \leq 10 \times 10^{-3}$ (Girton and Sanford, 2003; Peters and Johns, 2006). Here, a quadratic bottom drag formulation with an intermediate drag coefficient of $C_d = 5 \times 10^{-3}$ is used to incorporate the bottom shear stress.

3.2. Turbulence models

Warner et al. (2005) incorporated the “generic length scale algorithm” in ROMS, which allows the use of different turbulence closures by changing the coefficients in the equations (Umlauf and Burchard, 2003). The first equation in the generic length scale (GLS) scheme is for the turbulent kinetic energy, k , and the second one is for a generic parameter, ψ , which is used to calculate the turbulent length scale, l . The GLS equations are

$$\frac{\partial k}{\partial t} + U_i \frac{\partial k}{\partial x_i} = \frac{\partial}{\partial z} \left(\frac{K_M}{\sigma_k} \frac{\partial k}{\partial z} \right) + P + B - \varepsilon \quad (1)$$

$$\frac{\partial \psi}{\partial t} + U_i \frac{\partial \psi}{\partial x_i} = \frac{\partial}{\partial z} \left(\frac{K_M}{\sigma_\psi} \frac{\partial \psi}{\partial z} \right) + \frac{\psi}{k} (c_1 P + c_3 B - c_2 \varepsilon F_{\text{wall}}), \quad (2)$$

where σ_k and σ_ψ are the turbulence Schmidt number for k and ψ , respectively. P and B represent production due to shear and buoyancy as

$$P = -\langle u'w' \rangle \frac{\partial U}{\partial z} - \langle v'w' \rangle \frac{\partial V}{\partial z} = K_M M^2, \quad M^2 = \left(\frac{\partial U}{\partial z} \right)^2 + \left(\frac{\partial V}{\partial z} \right)^2, \quad (3)$$

$$B = -\frac{g}{\rho_0} \langle \rho'w' \rangle = -K_H N^2, \quad N^2 = -\frac{g}{\rho_0} \frac{\partial \rho}{\partial z}, \quad (4)$$

where N is the buoyancy frequency, M is the vertical shear, g is the gravitational acceleration, ρ_0 is the reference density, $\langle \cdot \rangle$ is the ensemble averaging operator, U and V are the mean horizontal velocity components, u' , v' , w' and ρ' are the turbulent velocity and density components, respectively. F_{wall} is the wall proximity function suggested by Mellor and Yamada (1982) and it is used only in Mellor–Yamada model and defined as

$$F_{\text{wall}} = \left(1 + E_2 \left(\frac{1}{\kappa} \frac{d_b + d_s}{d_b d_s} \right)^2 \right), \quad (5)$$

where $\kappa = 0.41$ is the von Kármán's constant and $E_2 = 1.33$. The parameters d_b and d_s are the distances from the bottom and surface, respectively. F_{wall} is one for the rest of the turbulence models.

In the framework of the ‘generic algorithm’ turbulent dissipation rate, ε , is defined according to

$$\varepsilon = (c_\mu^0)^{3+p/n} k^{3/2+m/n} \psi^{-1/n}, \quad (6)$$

where c_μ^0 is a coefficient based on experimental data for unstratified channel flow with a log-layer solution (Warner et al., 2005). The value of c_μ^0 changes according to which stability functions have been used. For instance, it is 0.5540 and 0.5270 for Canuto-A and Canuto-B, respectively. The definitions of generic parameter, ψ , turbulent length scale, l , and turbulent frequency, ω , are

$$\psi = (c_\mu^0)^p k^m l^n, \quad (7)$$

$$l = (c_\mu^0)^3 k^{3/2} \varepsilon^{-1}, \quad (8)$$

$$\omega = (c_\mu^0)^{-1} k^{1/2} l^{-1}. \quad (9)$$

In this study, three different two-equation turbulence closures are used. These are k - ε (Burchard and Baumert, 1995), k - ω (Umlauf et al., 2003), and the Mellor–Yamada level 2.5 scheme (Mellor and Yamada, 1982). Different closures can be obtained from Eqs. (1) and (2) by changing the coefficients. However, we use the original Mellor–Yamada model in a stand alone subroutine. The coefficients used in this study are taken from Warner et al. (2005) and listed in the Table 1. The parameter c_3 has two values; one for unstable stratification positive, c_3^+ and one for stable stratification negative, c_3^- .

In the hydrostatic primitive equations resulting from Reynolds averaging of the Navier–Stokes equations, there are Reynolds stress terms (i.e. $\langle u_i' u_j' \rangle$). If the transport equations for the Reynolds stresses are derived, third-order moments and pressure strain correlations are encountered. This is the famous *turbulence closure problem* since the number of unknowns are more than the number of equations. One way to close the system is to parameterize the third-order moment and pressure strain correlation terms. After the parameterization of these terms, so-called stability functions can be derived algebraically from the Reynolds stresses equations for steady state, homogeneous conditions. The stability functions describe the effect of shear and stratification. ROMS provides three different stability functions: KC (Kantha and Clayson, 1994), Canuto-A, CA, and Canuto-B, CB, (Canuto et al., 2001), which are used to calculate the eddy viscosity, K_M , and the eddy diffusivity, K_H as

$$K_M = c\sqrt{2kl}S_M + \nu, \quad K_H = c\sqrt{2kl}S_H + \nu_\theta, \quad (10)$$

where c is a coefficient with a value of $c = 1.0$ for Galperin et al. (1988) stability functions and $c = \sqrt{2}(c_\mu^0)^3$ for CA and CB. S_M and S_H are the stability functions, and ν and ν_θ are the molecular viscosity and diffusivity, respectively. Stability functions depend on k , l , N , and M . For detailed information about the stability functions, the reader is referred to Warner et al. (2005) and Burchard and Bolding (2001). Recently, Canuto et al. (2007) proposed a new model without any cut-off Richardson number in the stability functions, which is not included here but one that deserves investigation as well.

In addition to these three closures, the K-profile parameterization (KPP) and a modified k - ε turbulence closure validated by Peters and Baumert (2007) (hereafter PB07) have been used. KPP is

Table 1
Coefficients used in k - ε , k - ω and MY2.5 closures

	k - ε	k - ω	MY2.5
p	3.0	-1.0	0.0
m	1.5	0.5	1.0
n	-1.0	-1.0	1.0
σ_k	1.0	2.0	2.44
σ_ψ	1.3	2.0	2.44
c_1	1.44	0.555	0.9
c_2	1.92	0.833	0.5
c_3^+	1.0	1.0	0.9
c_3^-	-0.4	-0.6	0.9

employed since most of the general circulation ocean models have this parameterization and it is widely used in the community. The PB07 closure does not contain separate stability functions. It rather uses, as an independent function of the gradient Richardson number, only their ratio, turbulent Prandtl number:

$$Pr_t = \frac{K_M}{K_H} = \frac{S_M}{S_H}. \quad (11)$$

In PB07, the turbulent Prandtl number depends on the Richardson number (Schumann and Gerz, 1995) as follows:

$$Pr_t = Pr_0 \exp\left(\frac{-Ri_g}{Pr_0 Ri_f^\infty}\right) + \frac{Ri_g}{Ri_f^\infty}, \quad (12)$$

where Ri_g is the gradient Richardson number, $Pr_0 = 0.63$, and $Ri_f^\infty = 0.2$. In this approach, the eddy viscosity and diffusivity are calculated from

$$K_M = \pi^{-2} \frac{k^2}{\varepsilon}, \quad K_H = \frac{K_M}{Pr_t}. \quad (13)$$

In order to provide a perspective of differences between the turbulence models, the inverse of turbulent Prandtl number, Pr_t^{-1} , is plotted versus the gradient Richardson number, Ri_g , in Fig. 3. The most striking feature in this plot is that CA, CB, and PB07 almost coincide around $Ri_g = 0.25$. The Galperin et al. (1988), G88 and Kantha and Clayson (1994), KC stability functions used in MY2.5 cause turbulence to collapse for $Ri_g \geq 0.19$ and $Ri_g \geq 0.23$, respectively. CA and CB also have cut-off Richardson numbers, $Ri_c = 0.847$ for CA and $Ri_c = 1.02$ for CB (Burchard and Bolding, 2001). At $Ri > Ri_c$ diffusivity and viscosity assume background values (i.e. $K_H \sim 10^{-5} \text{ m}^2 \text{ s}^{-1}$ and $K_M \sim 10^{-4} \text{ m}^2 \text{ s}^{-1}$). Thus, turbulent Prandtl number for CA, CB, G88, KC and KPP become $Pr_t = 10$ for large Richardson numbers.

Stationary Richardson number Ri_{st} (Umlauf and Burchard, 2003) is another important parameter in two-equation models, which controls the entrainment in stably-stratified shear flows. Ri_{st} can be evaluated using

$$Ri_{st} = \frac{S_M}{S_H} \frac{c_2 - c_1}{c_2 - c_3}. \quad (14)$$

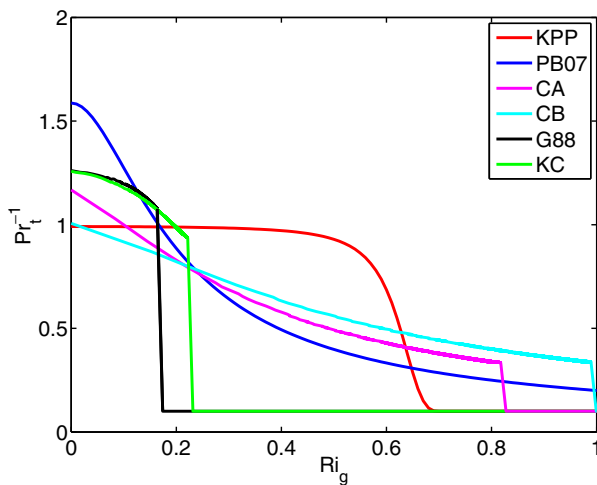


Fig. 3. Inverse Prandtl number, Pr_t^{-1} , versus gradient Richardson number, Ri_g , for different turbulence models. Quasi-equilibrium versions of CA = Canuto-A stability function, CB = Canuto-B stability function, G88 = Galperin stability function, PB07 = modified $k-\varepsilon$ model, KC = Kantha–Clayson stability function.

Table 2

Stationary Richardson numbers for different turbulence closures and stability functions

Turbulence closure	Stability function	Ri_{st}
$k-\varepsilon$	CA	0.303
$k-\omega$	CA	0.265
$k-\omega$	CB	0.251
$k-\varepsilon$	CB	0.278
$k-\varepsilon$	PB07	0.220
MY2.5	G88	None
MY2.5	KC	0.210

Stationary Richardson numbers for different closures and for different stability functions are shown in Table 2. The MY2.5 model exhibits no homogeneous and stationary solution, and thus no stationary Richardson number, if the original parameters are used (Baumert and Peters, 2000). However, Mellor–Yamada using KC stability function and $c_3 = 2.55$ has a stationary Richardson number which is very close to $Ri_c = 0.23$.

4. List of experiments and evaluation strategy

A total of nine experiments are conducted with different turbulence closure models and stability functions (Table 3). These models are standard $k-\varepsilon$ with CA and CB stability functions, standard $k-\omega$ with CA and CB stability functions, K-profile parameterization (KPP), the Mellor–Yamada level 2.5 scheme (MY2.5) with G88 and KC stability functions, and $k-\varepsilon$ with PB07 turbulent Prandtl number. Additionally, a control experiment is conducted with K_M and K_H set to zero. The objective of the control experiment is to investigate the flow dynamics when the vertical transport is limited. We will try to address the question how $K_M = K_H = 0$ will affect the overflow in the sense of mixing and flow patterns. The main task of all experiments is to explore which turbulence model leads to the best agreement with REDSOX-1 observations. In all the simulations, we use zero explicit horizontal numerical viscosity but just the implicit viscosity built into the third-order, upstream-biased advection operator (Shchepetkin and McWilliams, 1998). The implicit viscosity is such that the effective Reynolds number at that grid resolution takes the largest value possible while still ensuring stability.

Two different approaches can be followed in evaluating the performance of turbulence closure models (Sagaut, 2005). The first approach is to compare the primary variables of prognostic turbulence closure equations to those from measurements. These variables can be the turbulent kinetic energy k , its dissipation rate ε , or the eddy viscosity K_M . This kind of approach (e.g., Peters and Baumert, 2007; Arneborg et al., 2007) requires the availability of adequate turbulence observations which are quite rare. The second approach is to compare simulated water temperature, salinity, and

Table 3

List of experiments, consisting of different turbulence closures, stability functions; CA = Canuto-A, CB = Canuto-B, G88 = Galperin, KC = Kantha–Clayson stability functions

Experiment	Turbulence closure	Stability function
Exp1	$k-\varepsilon$	CA
Exp2	$k-\omega$	CA
Exp3	$k-\omega$	CB
Exp4	$k-\varepsilon$	CB
Exp5	KPP	none
Exp6	MY2.5	G88
Exp7	$k-\varepsilon$	PB07
Exp8	$K_M = K_H = 0$	None
Exp9	MY2.5	KC

velocity to observations. This approach is as important as the first since in oceanic simulations the primary variables are crucial. In fact, the two approaches are complementary to one another. In this study, we follow both avenues by comparing modeled salinity, temperature and velocity profiles and eddy diffusivity to those from REDSOX-1 observations.

The experiments are conducted on a Linux server with four AMD dual-core Opteron 865 processors (1.8 GHz) and 16 GB of RAM. All simulations are conducted on four processors and take approximately three days in real time for an integration time of 34 days.

5. Results

5.1. Description of the modeled overflow

A three-dimensional view of the propagation of the outflow is shown in Fig. 4. This view is complemented by Fig. 5, which depicts plan view of salinity distributions of the bottom layer of the Exp1 model run at four different times, from day 0 to 15. After the dense water is released at $t = 0$, it takes approximately one day to reach the bifurcation point of the northern and southern channels. At this point, the overflow flows into the northern channel first (Figs. 4a and 5b) and into the southern channel only later. This feature has also been observed in the REDSOX experiments. Matt and Johns (2007) mentioned that the flow into the southern channel is delayed because it has to overcome a sill 33 m above the floor of the northern channel. The resolution of this phenomena shows that our model resolution is sufficiently high. After reaching the bifurcation point, it takes the outflow five days to reach the Tadjura

Rift (Fig. 5c). In the Tadjura Rift, the two branches equilibrate at different depths; 800 m for the northern channel flow, and around 550 m southern channel flow (Fig. 6). Since the bottom layer in the sigma coordinates is plotted, the overflow appears to vanish in Fig. 5 at the edge of the Tadjura Rift. This is merely an artifact of the plot. The continuation of the plume lifting off the bottom is depicted in Fig. 6.

The plan view of the bottom layer in the control experiment is plotted in Fig. 7. The difference with respect to Fig. 5d is drastic. In Fig. 7 there is obvious lateral dispersion around SC. In the narrow NC the lateral dispersion is limited and thus there is somewhat better agreement with the observations than in the SC. Longitudinal sections of the control experiment (Figs. 17i and 18i) clearly shows the horizontal dispersion. There is high saline water between the NC and SC around the latitude 12.3° in the Fig. 7. Since vertical eddy diffusivity is set to zero, there is only background vertical diffusivity and probably some numerical mixing. Thus, the overflow cannot thicken enough to overcome the sill in front of the SC, therefore it goes directly to the NC. Bathymetry at the entrance of the NC allows the overflow to leak from the side walls. This process is a complex 3D dynamics which is beyond the scope of this paper. Lateral dispersion after leaking from the NC is due to topography. The main overflow pathways are not realistically reproduced in the control experiment.

5.2. Comparison of modeled and observed eddy diffusivity profiles

Next, modeled eddy diffusivity profiles from the northern and southern channels are compared with REDSOX-1 data. Peters and Johns (2005) estimate turbulence variables from turbu-

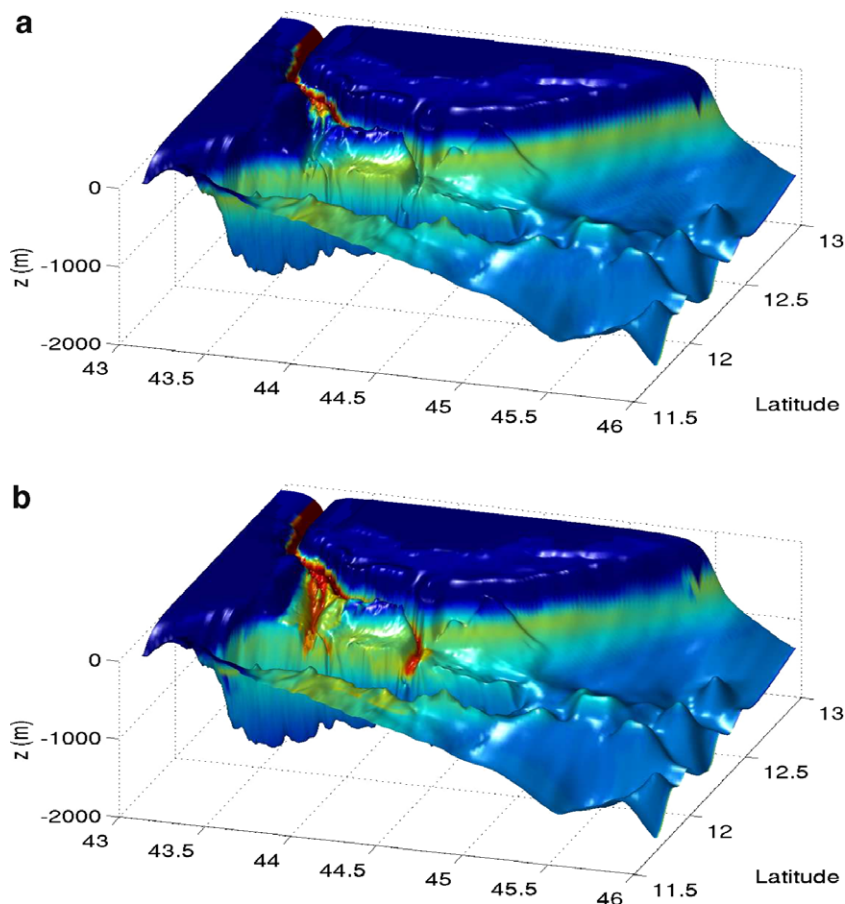


Fig. 4. 3D Salinity distribution of the bottom layer in Exp1 at $t = 1$ day, and $t = 15$ days. Blue ≈ 36 psu, Green ≈ 38 psu, Red ≈ 40 psu.

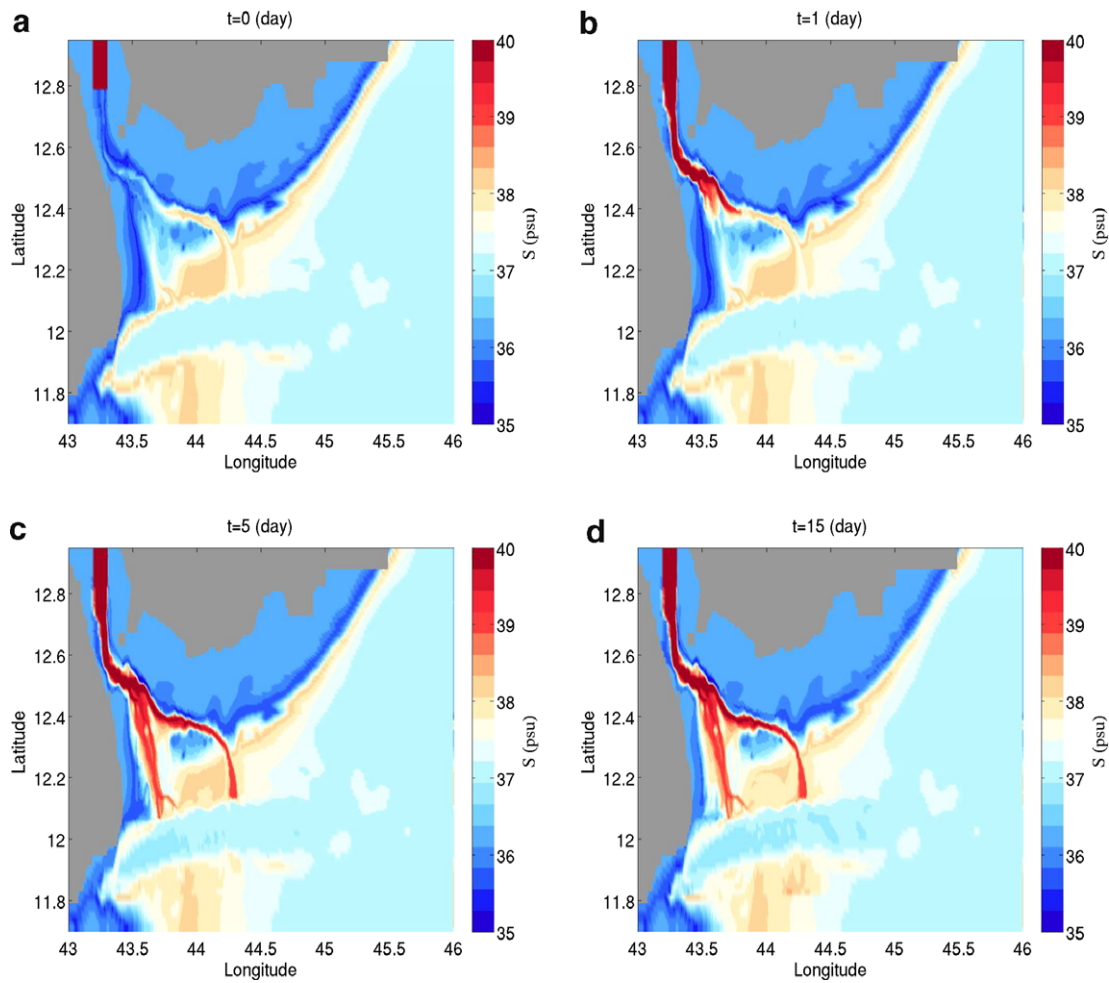


Fig. 5. Salinity distribution of the bottom layer as function of longitude and latitude of the Exp1 model at times $t = 0, 1, 5,$ and 15 days.

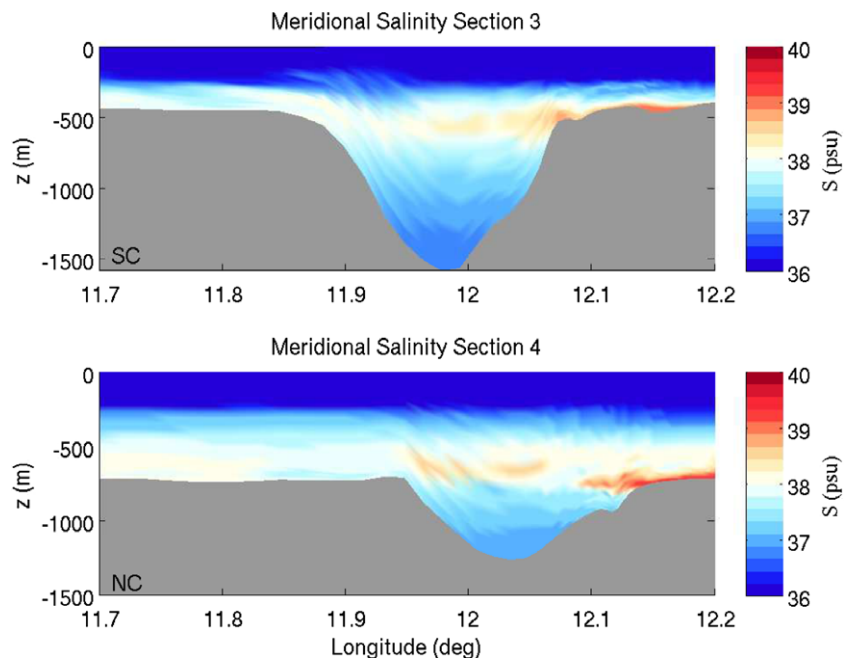


Fig. 6. Salinity distribution along the meridional Sections 3 and 4 at time $t = 30$ days (see Fig. 2), (upper panel) in the SC and (lower panel) in the NC.

lent overturning scales extracted from regular CTD profiles. Estimates of ε , K_M and K_H are provided only as averages over the IL.

We follow the definition of the IL given in Peters and Johns (2005) and compute average IL eddy diffusivities as illustrated

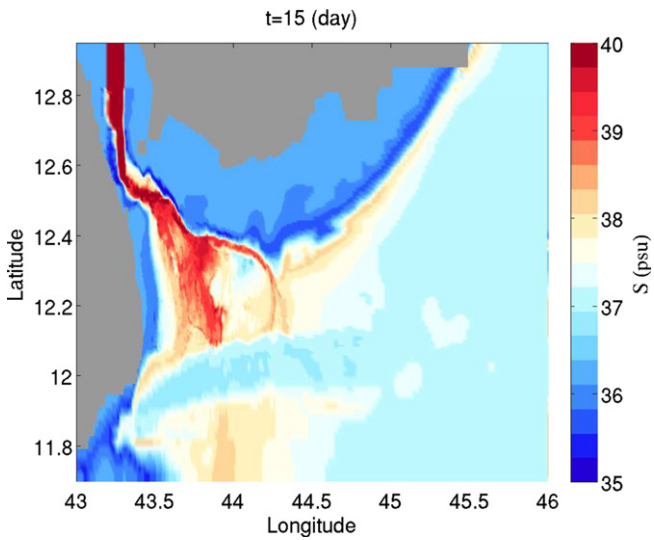


Fig. 7. Bottom salinity from control run, Exp8, at $t = 15$ days. Note the horizontal spreading especially around the SC.

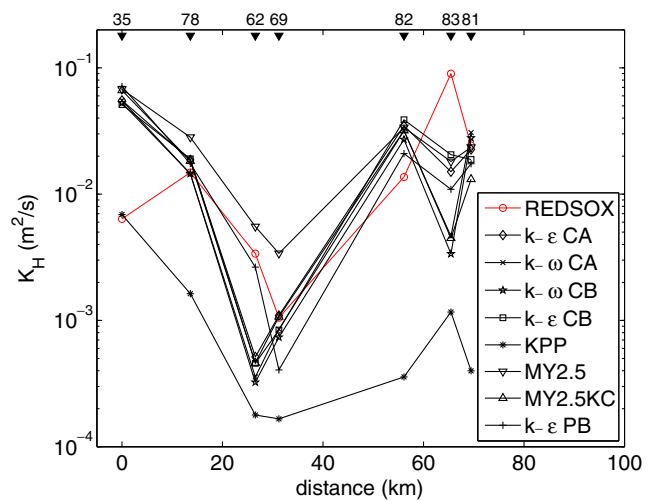


Fig. 9. Modeled and observed average eddy diffusivity in the IL of the northern channel overflow. Distances along the channel are measured from REDSOX-1 station 35.

in an example in Fig. 8. In the model output, the eddy diffusivity has a minimum at the velocity maximum. REDSOX-1 observations also imply this phenomena (see Peters and Johns (2005)).

In the NC, REDSOX-1 stations 35, 78, 62, 69, 82, 83, and 81 (Fig. 1) are used to compute the eddy diffusivity in the IL (Fig. 9). Even though the observations as well as modeled data show large variations along the channel, it is clear that K_H increases near the end of the northern channel. All the models except KPP capture this increase. Mean values of the eddy diffusivity of all the stations are around $2 \times 10^{-2} \text{ m}^2 \text{ s}^{-1}$ in the observation and in the models except for KPP. Such high values of K_H are common in swift, stratified shear flows (Wesson and Gregg, 1994; Peters, 1999). These average values are three orders of magnitude larger than the background mixing encountered in the ocean away from rough topography (Polzin et al., 1997).

In the SC, REDSOX-1 stations 29, 56, 28, 44, 27, and 19 (Fig. 1) are used to compute the eddy diffusivity in the IL (Fig. 10). In the first 20 km of the SC the values are comparable to the NC values, but at greater distances, mixing is reduced and eddy diffusivity values are lower than in the NC in a thinner and slower flow. The main reason for the reduction in the flow speed and mixing appears to be that the SC is getting wider near the exit. Mean values of the eddy diffusivity of the models and observation are around $5 \times 10^{-3} \text{ m}^2 \text{ s}^{-1}$. Although these average values are one order of magnitude smaller than the NC values, they are still large compared to ocean background mixing.

The differing levels of K_H in different turbulence models have implications for $T-S$ profiles which we re-examine further below. From Figs. 9 and 10, it is clear that KPP has relatively low K_H values except in the SC at 30 km. This indicates low mixing in the IL. In contrast, MY2.5 with G88 shows relatively high K_H values indicat-

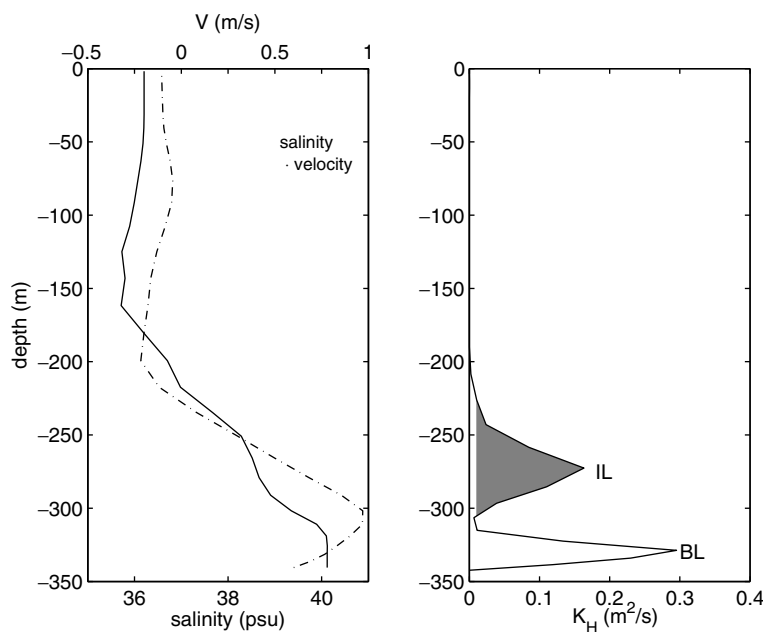


Fig. 8. Profiles of salinity, velocity (left panel), and eddy diffusivity (right panel) at station 35 from Exp7. The shaded area is the layer referred to as the IL. The mean eddy diffusivity, \bar{K}_H , of this area is compared with ocean observations.

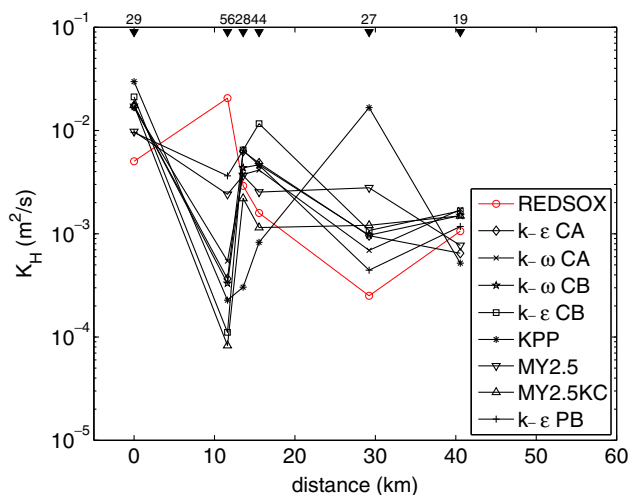


Fig. 10. Modeled and observed average eddy diffusivity in the IL of the southern channel overflow. Distances along the channel are measured from REDSOX-1 station 29.

ing strong mixing in the IL. The rest of the models have similar K_H values. This suggests that similar results are to be expected for simulated velocity, salinity and temperature fields as well.

5.3. Comparison of modeled and observed salinity and temperature profiles

Simulated salinity (S) and temperature (T) profiles are compared with the REDSOX-1 observations at four stations each, in the northern and the southern channel. The stations chosen are 35, 58, 37, and 81 in the northern channel and 29, 28, 57, and 19 in the southern channel (for the locations of the stations see Figs. 1 and 2). Salinity and temperature profiles from our eight experiments are compared with the REDSOX data in Figs. 11–14. We compare the observations with time averages of the model profiles. Time averages are computed as $\bar{X} = (\tau_2 - \tau_1)^{-1} \int_{\tau_1}^{\tau_2} X dt$ with $\tau_1 = 20$ days and $\tau_2 = 30$ days. Here, X stands for T and S . The structure of the temperature profiles (Figs. 13 and 14) from different experiments is similar to that of salinity (Figs. 11 and 12). Therefore, the following comparisons and discussions are based on salinity profiles alone. In the observations, there is a distinct high salinity layer at 150 m depth at the entrances of the channels (stations 35 and 29). It is thought that the formation of this saline water mass is related to tidal stirring within the BAM Strait (Matt and Johns, 2007). Herein, the flow within the Strait of BAM is not modeled. Discrepancy at station 81 is due to the initial salinity profile (see the dashed line in Fig. 11).

The first noticeable feature is that all the models capture the vertical structure of the overflow consisting of BL and IL. There are slight differences between the models, for instance, KPP has a thin IL compared to the others in both channels. This feature can be clearly seen in temperature profiles (cyan curves in Figs. 13 and 14). In MY2.5 with the Galperin et al. (1988) stability functions, the salinity in the BL is small (green curves¹ in Figs. 11–14). Near the exit of the NC, MY2.5 with G88 has a thick IL as a result of excessive mixing of the BL with the overlying water (ST81 in Fig. 11). Five models ($k-\epsilon$ CA, $k-\omega$ CA, $k-\omega$ CB, $k-\epsilon$ CB, MY2.5KC) show similar salinity profiles. These findings are consistent with implications from K_H levels discussed in Section 5.2. The model PB07 exhibits reasonable agreement compared to the observations just like the other five models.

¹ For interpretation of color in Figs. 1–7, 9–16, the reader is referred to the web version of this article.

5.4. Comparison of modeled and observed velocity profiles

Comparisons of the modeled and observed velocity profiles at selected stations along the northern and the southern channels are shown in Figs. 15 and 16. The horizontal velocity components, u and v , are projected into the flow direction so that only one streamwise velocity component is shown. The modeled velocities are also time-averaged between model days 20 and 30. The flow direction from the other experiments is also used for the control experiment. However, as the flow spreads laterally in the control case, maximum velocities of the control experiment are higher than in the observations; since there is no vertical momentum transfer the flow undergoes excessive acceleration.

Modeled velocity profiles are similar to the observations in the northern channel; the maximum velocities in all models are approximately 0.9 m s^{-1} . Among the output from different closures the comparatively small velocities from MY2.5 with G88 toward the end of the NC stand out (green curve at station 81 in Fig. 15).

In the southern channel, modeled maximum velocities are slightly larger than those of observation. There is a good agreement with REDSOX-1 data at the end of the southern channel (station 19 in Fig. 16). Maximum velocities in all models are approximately 0.6 m s^{-1} , and maximum velocity in the observation is around 0.4 m s^{-1} .

The model velocity profiles are highly sensitive to the boundary conditions at Bab el Mandeb. We have modified these conditions such as to accurately reproduce the flow at station T0, which is downstream from the boundary conditions at BAM but upstream of the channel sections where we probe the model performance. If, for instance, velocities at T0 are even modestly too large, the flow in the SC can become as swift as 1.1 m s^{-1} .

It cannot be expected that the model simulations match the observations perfectly. The CTD/LADC profiles represent an incoherent, possibly aliased survey taken in a time-variable flow field see Fig. 9 in Peters et al. (2005b). Reasonable agreement with REDSOX-1 observations is found in both channels for all models.

5.5. Error analysis of different turbulence closures

In this section, we examine salinity deviations between the numerical experiments and the observations. First, salinity sections are compared visually and qualitatively, and then the deviations are quantified.

Salinity distributions along Sections 1 and 2 introduced in Fig. 2 are plotted for the different experiments and the REDSOX observations in Figs. 17 and 18, respectively. It is clearly seen in the observations (Fig. 17a) that the overflow water in the northern channel is denser than that in the southern channel. This pattern is adequately captured by all closures except MY2.5 with G88. There is not enough dense water in the southern channel in MY2.5 with G88. Experiments 1–4 show very similar salinity sections to each other (Figs. 17b, c, g, and h). In Section 2, mixing is high for Exp6 and bottom, dense flow signal becomes weak (Fig. 18i). On the contrary, KPP does not mix enough in the SC (Fig. 18f). This can be also seen in individual salinity profiles in the SC (Fig. 12). Section 2 is more important than Section 1, since it is far away from the bifurcation point. In Section 2, MY2.5 with G88 and KPP deviate much more from the observed S than the other closures. Dense water is absent in the channels in the control run (Fig. 18j), since the control experiment spreads horizontally. Further, there is high saline water between the channels (red stripes between the channels in Figs. 17j and 18j) not seen in the observations. There is a distinct difference between MY2.5KC and MY2.5 with G88 (Fig. 18d and

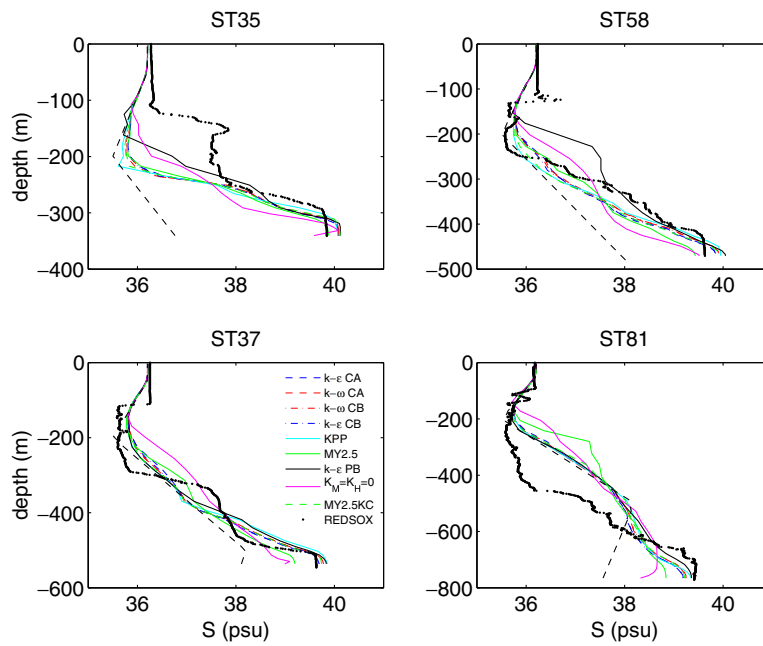


Fig. 11. Comparison of salinity profiles from different models and REDSOX-1 observations in the northern channel. The dashed lines are initial profiles.

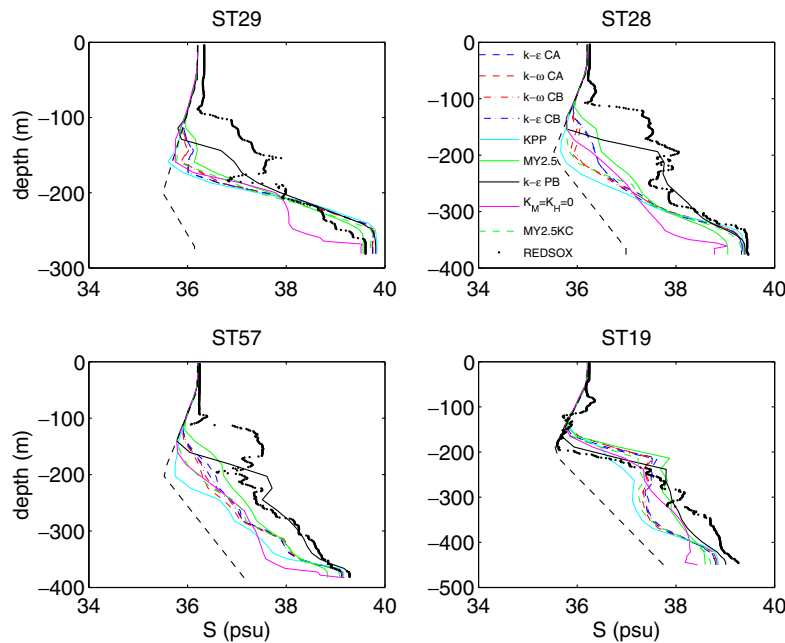


Fig. 12. Comparison of salinity profiles from different models and REDSOX-1 observations in the southern channel. The dashed lines are initial profiles.

18i), the former shows reasonable agreement with the observations and the other models.

We will now quantify the model deviation from the observed S and try to answer the question if some closures perform significantly better or worse than the others. This is a difficult question because of the uncertainty in the sparse observations. For instance, the observed maximum salinity in Section 2 is 39.55 psu while the maximum is only 38.6 psu in the MY2.5 with G88 simulations. Does this single out MY2.5 with G88 for poor performance? Three stations (38, 81, and 101 in Fig. 1) were taken near the lower end of the NC at different times. We compute a mean salinity profile, \bar{S} , from these stations along with its standard deviation, σ , (Fig. 19).

Since the BL is well-mixed, it is sufficient to analyze the statistics of the BL mean, \bar{S} , in observations and simulations. Results appear in Table 4. We take two standard deviations as confidence bounds of the observations. Only KPP and the $k-\epsilon$ PB07 fall into the confidence bounds of the REDSOX data (italicised values in REDSOX row in Table 4). Maximum salinities from $k-\epsilon$ CA, $k-\omega$ CA, $k-\omega$ CB and $k-\epsilon$ CB are 0.1 psu smaller than the bottom limit of REDSOX-1 values. The maximum value of MY2.5 with G88 is still smaller by 0.4 psu than the bottom limit of the REDSOX-1 values. We conclude that the MY2.5 with G88 scheme falls outside of the variance range of the REDSOX data at the lower end of the NC. However, MY2.5KC is significantly better than MY with G88 stability

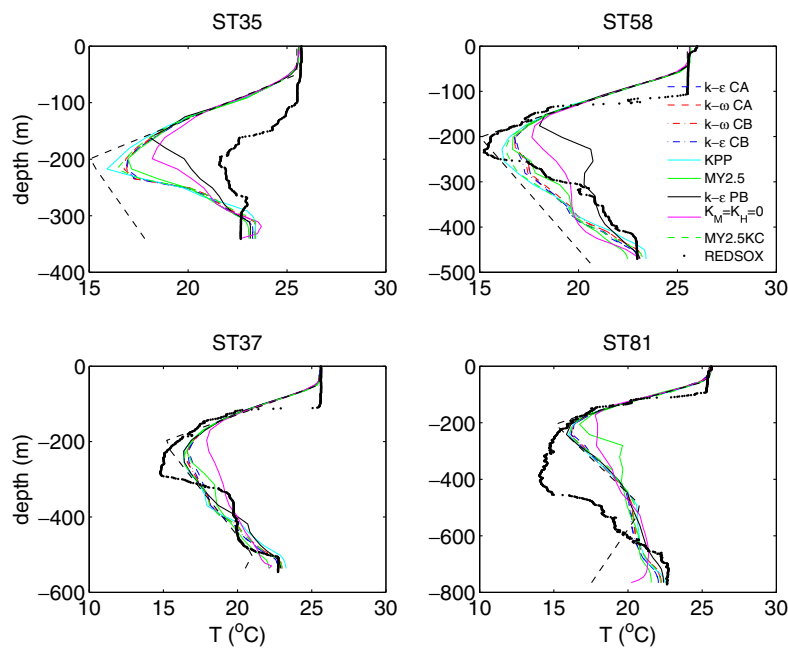


Fig. 13. Comparison of temperature profiles from different models and REDSOX-1 observations in the northern channel. The dashed lines are initial profiles.

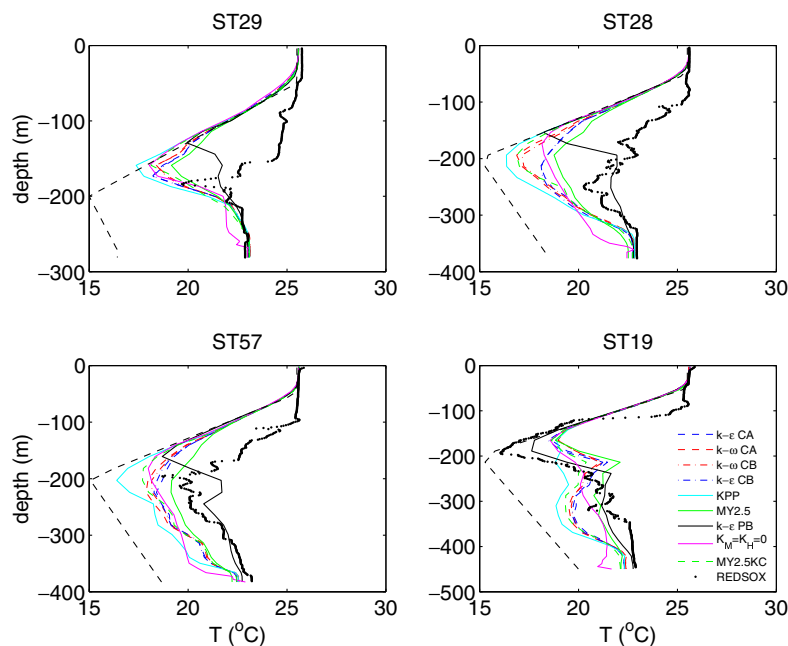


Fig. 14. Comparison of temperature profiles from different models and REDSOX-1 observations in the southern channel. The dashed lines are initial profiles.

functions in this analysis. MY2.5KC is only 0.16 psu smaller than the bottom limit of REDSOX-1 values. This value is very similar to the other model's performance. This clearly shows that stability functions have a clear impact on the overall performance of the MY2.5 turbulence model.

Given the stratification in the IL, comparing simulated and observed mean salinities from the IL makes little sense. The salinity variance in the IL is much larger in the observations than in any of the model runs. The large observed variability of S in the IL is probably caused by time variations in flow and mixing. These cannot be captured in the model since its boundary forcing is constant and there is no wind forcing.

In order to quantify the difference between the observations and the results of the different models, an error function is defined as

$$\text{Error} = \frac{1}{n} \sum_{i=1}^{i=n} \frac{1}{\Delta S} \sqrt{\sum_{j=1}^{j=M^i} [\bar{S}_{\text{model}}^i(j) - S_{\text{obs}}^i(j)]^2 / M^i}, \quad (15)$$

where \bar{S}_{model}^i is the time-averaged model output, S_{obs}^i is the observed salinity at station i , M^i is the number of vertical sampling points at each data station, n is the number of stations. Section 1 is made by interpolating 11 REDSOX-1 stations, these stations are 67, 58, 61, 60, 59, 70, 71, 72, 73, 74, 75, 76. Therefore, we used these stations

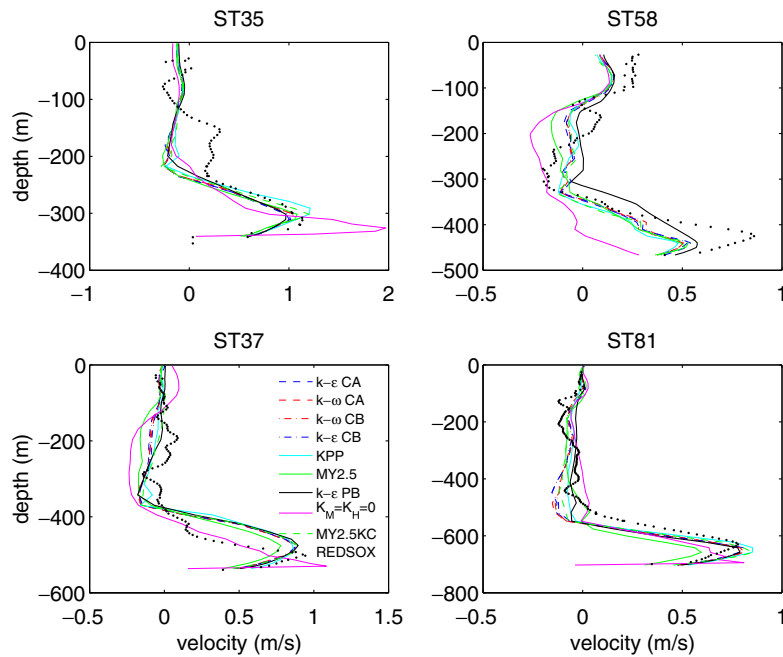


Fig. 15. Comparison of the streamwise velocity profiles from different models and REDSOX-1 observations in the northern channel.

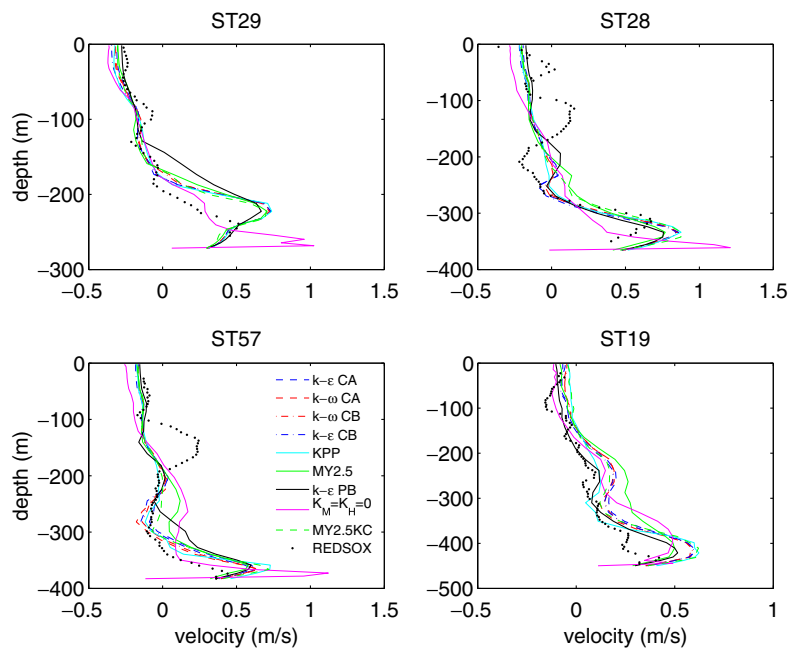


Fig. 16. Comparison of the streamwise velocity profiles from different models and REDSOX-1 observations in the southern channel.

to calculate the root mean square error (Error) for Section 1. Section 2 is made by interpolating 15 REDSOX-1 stations, these stations are 07, 08, 09, 10, 11, 12, 13, 14, 15, 16, 17, 18, 19, 20, 21, 22, 23, 24. We also used these stations to calculate the Error for Section 2. Thus, number of stations, n , is 12 for Section 1 and 18 for Section 2. Salinity deviations are normalized by a salinity range of $\Delta S = 3.5$ psu, since only the overflow plume, defined by a salinity interface larger than 36.5 psu, is used to compute the deviation. Results are shown in Table 5, salinity deviations at Section 1 are larger than at Section 2, since there is the intrusion layer in the observations (Fig. 17a). The models cannot capture this layer as already mentioned above. Salinities from KPP, MY2.5 with G88 and the control experiment

have the higher deviations from the observations at both sections than the other experiments which have smaller, similar errors.

As a further and final test of the model performance, we calculate the mass transport of different salinity classes. We divide the overflow into ten equal salinity classes from 36.5 to 39.5 psu and we calculate the mass transport, $\int u dz$, of each class. Fig. 20 depicts the mass transport of the different models at stations 81 and 19 near the lower ends of the NC and SC, respectively. In the NC, only $k-\epsilon$ models have comparable transports with the observed transport (Fig. 20a) at the maximum salinity class (i.e. $39.2 < S \leq 39.5$ psu). MY2.5 with G88 and control cases have zero transport for that class since maximum salinities in these models

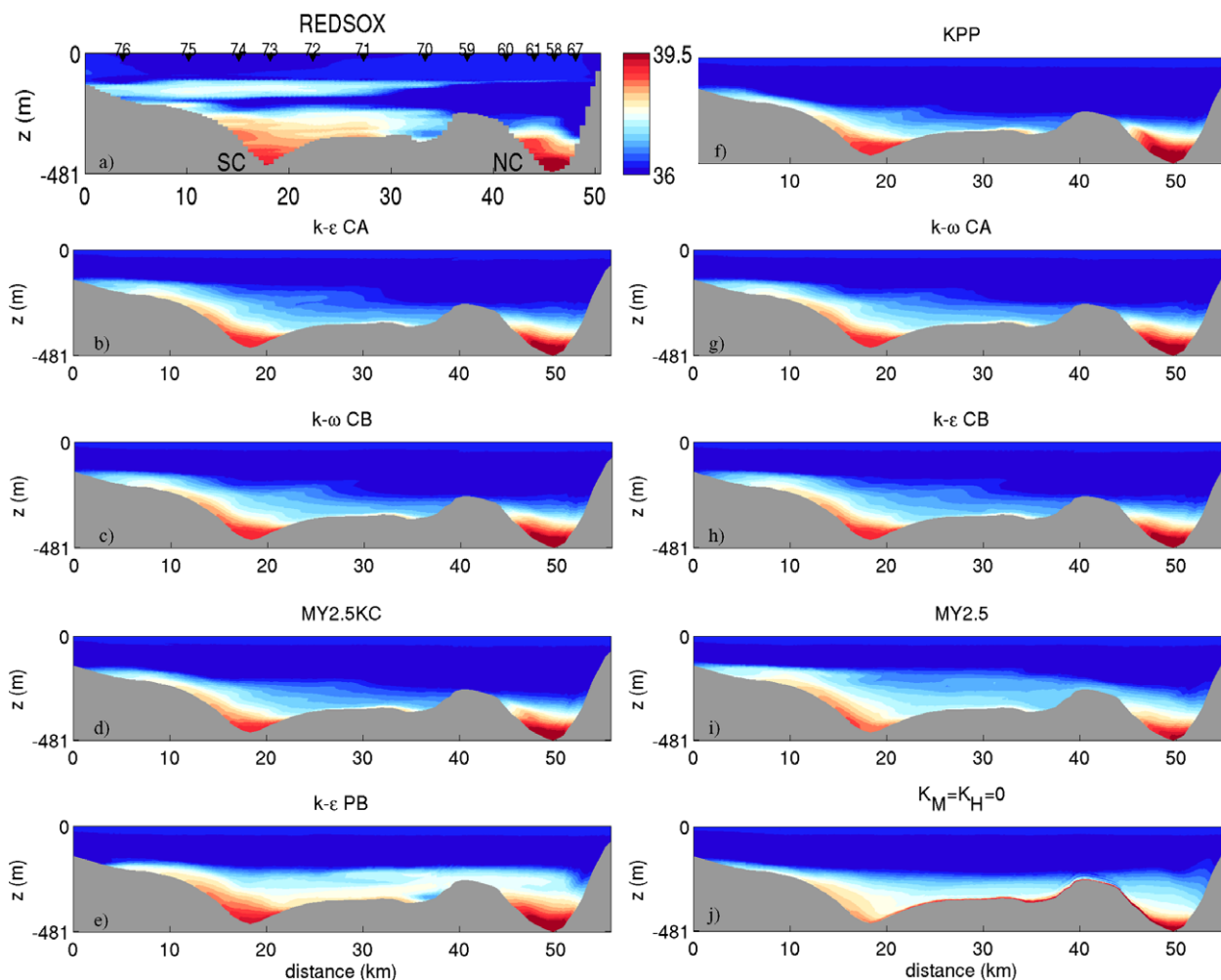


Fig. 17. Salinity distribution of all model experiments and REDSOX-1 data along Section 1 (see Fig. 2 for the position of the section).

are less than 39.2 psu. KPP and two $k-\omega$ models behave similarly to each other by transporting the same salinity classes. In the SC, only $k-\epsilon$ PB07 and REDSOX-1 transport the second most dense class (i.e. $38.9 < S \leq 39.2$ psu). MY2.5 with G88 and control cases again have zero transport at denser classes, and these models transport intermediate salt classes compared to the other models (Fig. 20b). For instance, the control experiment has the highest transport at the class where salinity falls between 38.0 and 38.3 psu. Also, MY2.5 with G88 has two peaks at the classes where salinity falls between 37.7 and 38.0 psu, and between 38.3 and 38.6 psu.

5.6. Explicit vs implicit diffusion

Given that the mixing in the Red Sea overflow is rather subtle because of small slopes, as emphasized in previous modeling studies by Özgökmen et al. (2003), Chang et al. (2008) and Ilıcak et al. (2008), it is of interest to investigate how much of the mixing relies on the turbulence closures explicitly, and how much is due to numerical truncation errors (implicit or artificial mixing). As outlined above, not only have we taken the necessary precautions by using the highest accuracy techniques available in this model, combined with fairly high spatial resolution, but also the fact that model results differ in response to different mixing models indicates that we should anticipate that implicit diffusion should be much smaller than explicit diffusion. Nevertheless, some degree of quantification of implicit mixing is desirable.

To this end, two parallel experiments are conducted by releasing a volume of passive tracer with a concentration value of 1 from the north-west corner of the domain, where we release the overflow. The ambient is initialized with passive tracer concentration of zero. The initial tracer volume with concentration 1 is approximately 2% of the control volume. Two sets of experiments are conducted by integrating the model equations with the passive tracer. In one case, the tracer is subject to the same eddy diffusivity as calculated for Exp4 configuration in full-developed overflow case. In the other case, both the eddy and background diffusivities for the tracer are set to zero, so that mixing occurs only due to numerical artifacts. Ideally, the initial distribution of concentration should remain constant in time, in this case.

The probability distribution function of the two cases after 3 days of integration are shown in Fig. 21. We conclude that while there is some implicit mixing, it is significantly smaller than that introduced by the turbulence scheme.

6. Summary and conclusion

Deep and intermediate water masses, formed as overflows, are key processes for the ocean general circulation. Small-scale mixing in overflows cannot be represented explicitly in the general ocean circulation models. Thus, parameterizations are crucial for OGCMs. To date, gravity current problems have been extensively studied by diagnostic models and MY2.5 two-equation model. There are also

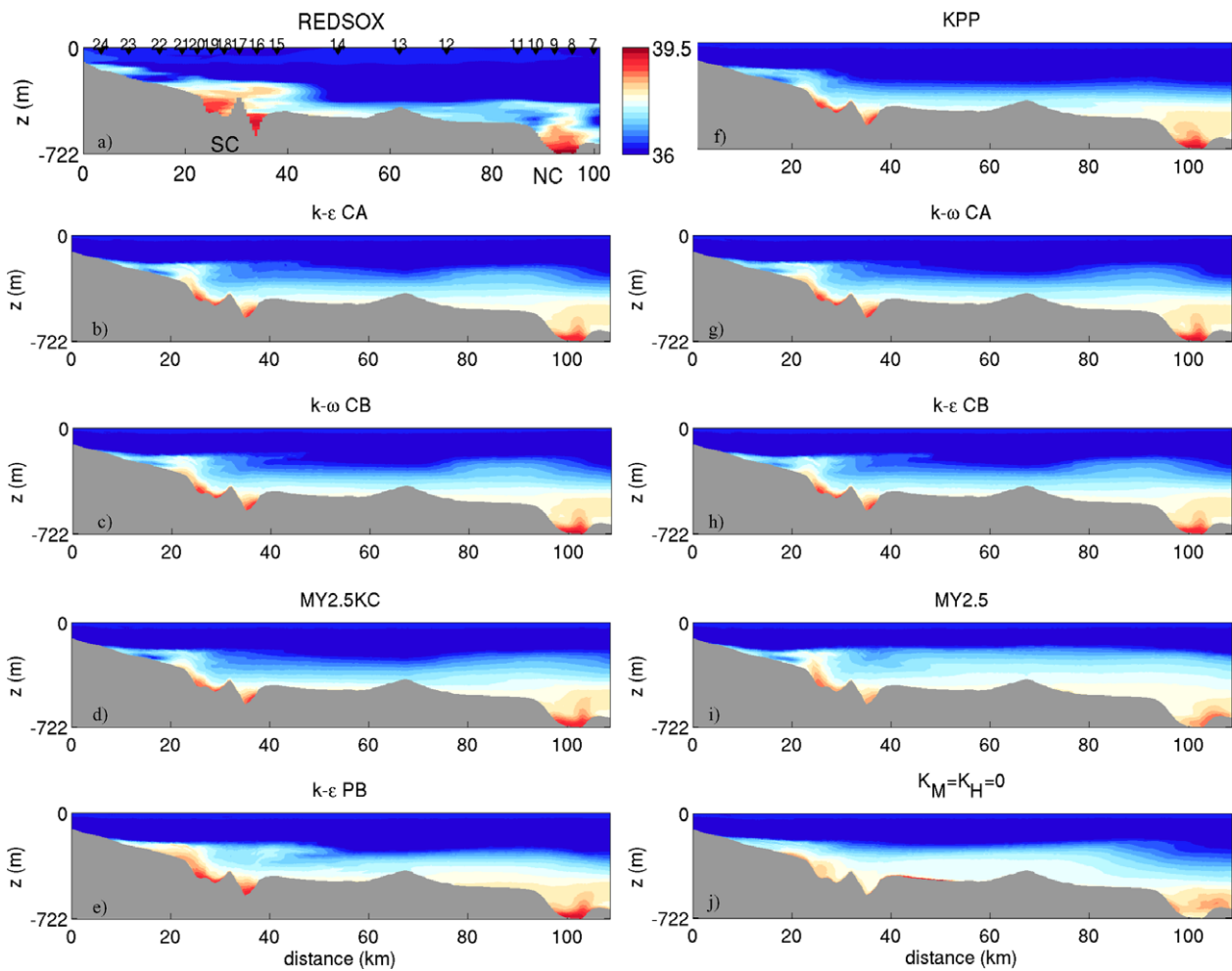


Fig. 18. Same as Fig. 17 but for Section 2.

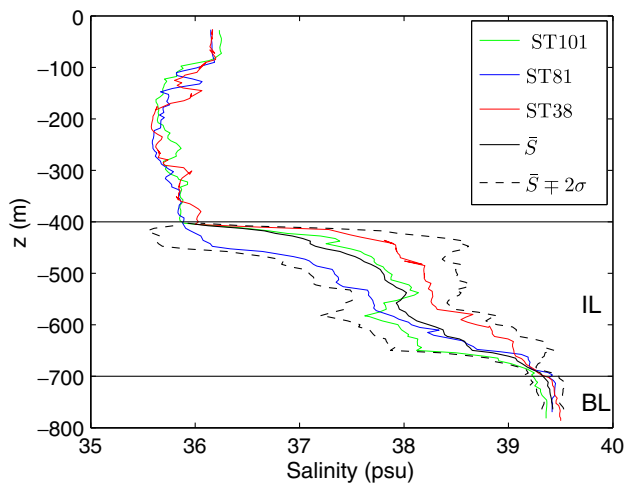


Fig. 19. Observed salinity profiles of stations 38, 81, and 101 together with the mean profile from these three stations and the 2-σ spread.

few recent studies with $k-\omega$ and $k-\epsilon$ two-equation models. All these models are validated by either LES studies or observational data.

In this study, we analyze the performances of a set of second-order turbulence models in a study of the Red Sea overflow using a hydrostatic circulation model. The turbulence models examined

Table 4

Mean salinity value, \bar{S} and its variance, σ , in the BL for different experiments and REDSOX-1 data

Experiments	\bar{S}	σ_{BL}	$\bar{S} - 2\sigma_{BL}$	$\bar{S} + 2\sigma_{BL}$
$k-\epsilon$ CA	39.128	0.0112	39.1056	39.1504
$k-\omega$ CA	39.198	0.0126	39.1668	39.2172
$k-\omega$ CB	39.197	0.0144	39.1682	39.2258
$k-\epsilon$ CB	39.126	0.0138	39.0984	39.1536
KPP	39.333	0.0248	39.2834	39.3826
MY2.5	38.787	0.069	38.649	38.925
$k-\epsilon$ PB07	39.282	0.0206	39.2408	39.3232
$K_M = K_H = 0$	38.563	0.205	38.153	38.973
MY2.5KC	39.098	0.018	39.062	39.134
REDSOX	39.397	0.05	39.297	39.497

Table 5

Average of normalized salinity errors (%) of different experiments at the Sections 1 and 2

Error (%)	Section 1	Section 2
$k-\epsilon$ CA	20.24	18.71
$k-\omega$ CA	20.11	18.87
$k-\omega$ CB	20.47	18.09
$k-\epsilon$ CB	20.92	18.27
KPP	25.51	22.06
MY2.5	23.01	25.43
$k-\epsilon$ PB07	20.61	16.60
$K_M = K_H = 0$	25.83	31.02
MY2.5KC	21.15	20.05

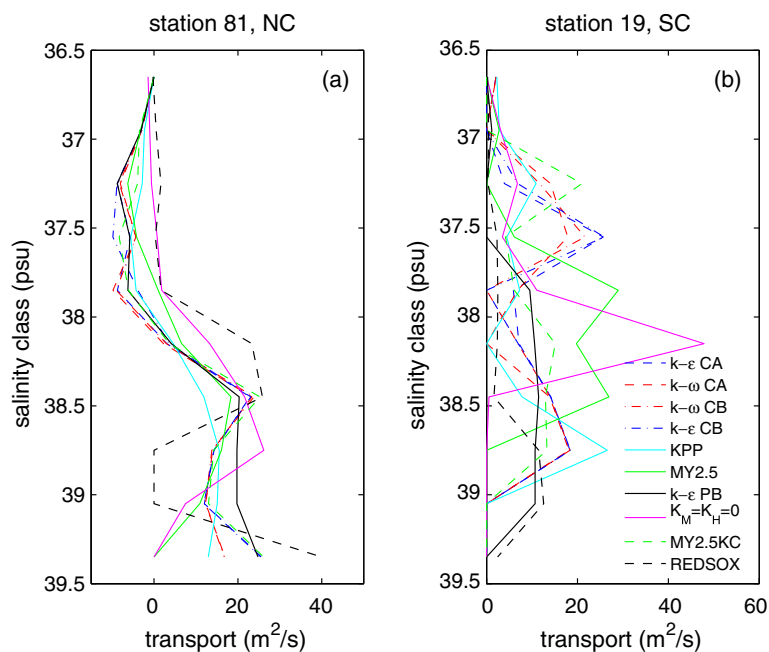


Fig. 20. Transport of the different salinity classes for different models and REDSOX-1 observations in the northern channel (left panel) and in the southern channel (right panel).

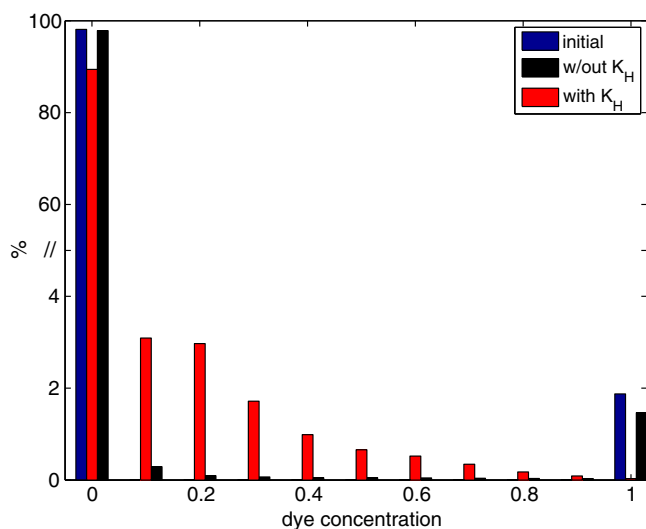


Fig. 21. The initial and final (after 3 days) probability distributions of the passive tracer concentration from cases with and without eddy diffusivity.

are conventional $k-\epsilon$, $k-\omega$, MY2.5, and a modified $k-\epsilon$. The model simulations are compared to temperature, salinity, velocity and eddy diffusivity observations from the 2001 REDSOX-1 cruise. As the overflow is contained in two narrow channels, we compare CTD/LADCP stations from the channels with corresponding model data. Model runs are integrated for it 34 days during which the flow becomes quasi-stationary. Time averages over model days 20–30 of primary variables (T, S, u) and secondary variables (K_H) are compared to the observations.

A set of nine experiments is conducted with different turbulence closures using different stability functions. These are conventional $k-\epsilon$ using CA and CB stability functions, $k-\omega$ using CA and CB stability functions, MY2.5 using G88 and KC stability functions, and a control experiment where $K_M = K_H$ is set to zero implicitly. Since it is widely used in the community, the KPP scheme is also tested

even though it is a diagnostic model. In addition, a modified $k-\epsilon$ model without stability functions but with Richardson number-dependent turbulent Prandtl number is also employed.

It has to be mentioned in here that numerical model setup such as high resolution around the channels, ambient stratification and/or correct forcing are as important as the vertical mixing schemes. In fact, Chang et al. (2008) found that the sensitivity of the simulations to choice of the vertical mixing scheme is small in Red Sea overflow. Thus, the Red Sea overflow might not be a highly discriminating case study to evaluate the performances of the different closures. Another fundamental problem is using small, sparse, and non-synoptic observational data sets to compare to the numerical simulations. Despite all these complications, we believe that this study is a needed step to distinguish better between the performances of turbulence models for overflow simulations.

In light of this information, the comparison of modeled and observed salinity, temperature, and eddy diffusivity distribution can be summarized as follows. All two-equation turbulence models are able to capture the vertical structure of the overflow consisting of the BL, which transports salty, dense water along the channels, and the IL, where most of the mixing and entrainment takes place. Mean eddy diffusivities in most closures are $O(10^{-2})$ in the NC and $O(10^{-3})$ in the SC. These values compare well with observational data. Eddy diffusivities are too small in KPP and too large in MY2.5 with G88. In consequence of the large K_H , the BL salinity becomes diluted in MY2.5 with G88. The control experiment exhibits poor results mainly because of horizontal dispersion of the flow beyond the confining channels.

Salinity deviations between model and observations are quantified along two sections across the overflow. KPP and MY2.5 with G88 produce the largest deviations from the observations and the modified $k-\epsilon$ exhibits the smallest deviations. The other five closures fall in between, showing deviations similar to one another. MY2.5KC displays better performance than the MY2.5 with G88. The main reason behind this is that the version with KC stability functions has a $Ri_{st} = 0.21$, whereas the one with G88 does not have a stationary Richardson number. The importance of Ri_{st} on entrainment in stably-stratified shear flows was emphasized

by Umlauf and Burchard (2003), and this seems to play a critical role in improving the performance of the MY2.5 model. We also experimented with two additional simulations such that $Ri_{st} = 0.25$ for $k-\epsilon$ CA and $k-\omega$ CA models, but they did not show significant improvements compared to the ones used in this study.

With respect to the ventilation of the deep ocean, all properties of gravity currents at their point of equilibration matter. That is, our model should adequately reproduce the transport of all salinity classes in the overflow. However, with respect to the lateral spreading along ocean basins of a saline water mass, the higher S classes, and especially the maximum S , matter most. On this background, success and failure of some closures of transporting the most saline and dense water are important. Only $k-\epsilon$ models transport the densest salinity class in the NC and only the modified $k-\epsilon$ transport the densest salinity class in the SC. KPP and $k-\omega$ models have correct salinity classes but weak transports compared to the observations. However, the control experiment and MY2.5 with G88 transport intermediate salinity classes in the NC and SC, therefore we can say that only $k-\epsilon$ models have successfully reproduced transport of the high salinity classes.

This study indicates that two-equation closures can perform well in the low- Ri_b , large shear setting of the overflows. Thus, it extends the range of applications for such closures to overflows. It is important to note that the quantitative performance relative to the observations of our model depends on much more than just the turbulence parameterization employed. Model results depend critically on such factors as horizontal and vertical resolution, ambient stratification, and proper forcing at the source of the overflow. Within such model sensitivities we find only modest differences in the performances of a range of tested two-equation closures, and overall reasonable agreement with the observations. In conclusion, we find that most turbulence closures lead to a satisfactory reproduction of the Red Sea overflow, within the temporal and spatial sampling uncertainties of the REDSOX data, provided that fairly high-resolution regional models are used.

Acknowledgements

We are grateful for the support of National Science Foundation via Grants OCE 0352047 and OCE 0620661. We thank Yeon Chang and Silvia Matt for providing the bottom topography data. Multi-beam echosoundings from the R/Vs Knorr, Maurice Ewing, L'Atalante were analyzed by Stephen Swift of Woods Hole Oceanographic Institution. We thank the two anonymous reviewers for their extremely constructive comments and suggestions, which greatly improved the manuscript.

References

- Arneborg, L., Fiekas, V., Umlauf, L., Burchard, H., 2007. Gravity current dynamics and entrainment – a process study based on observations in the Arkona basin. *J. Phys. Oceanogr.* 37, 2094–2113.
- Baines, P.G., 2001. Mixing in flows down gentle slopes into stratified environments. *J. Fluid Mech.* 443, 237–270.
- Baringer, M.O., Price, J.F., 1997. Mixing and spreading of the mediterranean outflow. *J. Phys. Oceanogr.* 27, 1654–1677.
- Baumert, H.Z., Peters, H., 2000. Second-moment closure and length scales for weakly stratified turbulent shear flows. *J. Geophys. Res.* 105, 6453–6468.
- Baumert, H.Z., Peters, H., 2004. Turbulence closure, steady state, and collapse into waves. *J. Phys. Oceanogr.* 34, 505–512.
- Beckmann, A., Haidvogel, D.B., 1993. Numerical simulation of flow around a tall isolated seamount. Part I: problem formulation and model accuracy. *J. Phys. Oceanogr.* 23 (August), 1736–1753.
- Bower, A.S., Fratantoni, D.M., Johns, W.E., Peters, H., 2002. Gulf of Aden eddies and their impact on Red Sea water. *Geophys. Res. Lett.* 29 (November), 21–1.
- Bower, A.S., Johns, W.E., Fratantoni, D.M., Peters, H., 2005. Equilibration and circulation of red sea outflow water in the western Gulf of Aden. *J. Phys. Oceanogr.* 35, 1963–1985.
- Burchard, H., Baumert, H.Z., 1995. On the performance of a mixed-layer model based on the $k-\epsilon$ turbulence closure. *J. Geophys. Res.* 100, 8523–8540.
- Burchard, H., Bolding, K., 2001. Comparative analysis of four second-moment turbulence closure models for the oceanic mixed layer. *J. Phys. Oceanogr.* 31, 1943–1968.
- Burchard, H., Lass, H.U., Mohrholz, V., Umlauf, L., Sellschopp, J., Fiekas, V., Bolding, K., Arneborg, L., 2005. Dynamics of medium-intensity dense water plumes in the Arkona Basin, Western Baltic Sea. *Ocean Dyn.* 55 (December), 391–402.
- Burchard, H., Janssen, F., Bolding, K., Umlauf, L., Rennau, H., 2008. Model simulations of dense bottom currents in the western baltic sea. *Cont. Shelf Res.* in press, doi:10.1016/j.csr.2007.09.010.
- Canuto, V.M., Howard, A.M., Cheng, Y., Dubovikov, M.S., 2001. Ocean turbulence. Part I: one-point closure model momentum and heat vertical diffusivities. *J. Phys. Oceanogr.* 31, 1413–1426.
- Canuto, V.M., Cheng, Y., Howard, A.M., Esau, I.N., 2007. Stably stratified flows: a model with No $Ri(cr)$. *J. Atmos. Sci.*
- Cenedese, C., Whitehead, J.A., Ascarelli, T.A., Ohiwa, M., 2004. A dense current flowing down a sloping bottom in a rotating fluid. *J. Phys. Oceanogr.* 34, 188–203.
- Chang, Y.S., Xu, X., Özgökmen, T.M., Chassignet, E.P., Peters, H., 2005. Comparison of gravity current mixing parameterizations and calibration using high-resolution 3d nonhydrostatic spectral element model. *Ocean Model.* 10, 342–368.
- Chang, Y.S., Özgökmen, T.M., Peters, H., Xu, X., 2008. Numerical simulations of the red sea outflow using hycom and comparison with redsox observations. *J. Phys. Oceanogr.* 38 (2).
- Dickson, R.R., Gmitrowicz, E.M., Watson, A.J., 1990. Deep water renewal in the northern North Atlantic. *Nature* 344, 848–850.
- Ellison, T.H., Turner, J.S., 1959. Turbulent entrainment in stratified flows. *J. Fluid Mech.* 6, 423–448.
- Ezer, T., 2005. Entrainment, diapycnal mixing and transport in three-dimensional bottom gravity current simulations using the Mellor–Yamada turbulence scheme. *Ocean Modell.* 9, 151–168.
- Ezer, T., 2006. Topographic influence on overflow dynamics: idealized numerical simulations and the faroe bank channel overflow. *J. Geophys. Res.* 111, 2002+.
- Ezer, T., Mellor, G., 2004. A generalized coordinate ocean model and comparison of the bottom boundary layer dynamics in terrain-following and in z-level grids. *Ocean Modell.* 6, 379–403.
- Galperin, B., Kantha, L.H., Hassid, S., Rosati, A., 1988. A quasi-equilibrium turbulent energy model for geophysical flows. *J. Atmos. Sci.* 45, 55–62.
- Geyer, F., Østerhus, S., Hansen, B., Quadfasel, D., 2006. Observations of highly regular oscillations in the overflow plume downstream of the faroe bank channel. *J. Geophys. Res.* 111, 12020.
- Girton, J.B., Sanford, T.B., 2003. Descent and modification of the overflow plume in the denmark strait. *J. Phys. Oceanogr.* 33, 1351–1364.
- Girton, J.B., Sanford, T.B., Käse, R.H., 2001. Synoptic sections of the denmark strait overflow. *Geophys. Res. Lett.* 28, 1619–1622.
- Gordon, A.L., Zambianchi, E., Orsi, A., Visbeck, M., Giulivi, C.F., Whitworth, T., Spezie, G., 2004. Energetics plumes over the western ross sea continental slope. *Geophys. Res. Lett.* 31 (21). Art. No. L21302.
- Hallberg, R., 2000. Time integration of diapycnal diffusion and richardson number dependent mixing in isopycnal coordinate ocean models. *Mon. Weather Rev.* 128 (5), 1402–1419.
- Hallworth, M.A., Huppert, H.E., Phillips, J.C., Sparks, S.J., 1996. Entrainment into two-dimensional and axisymmetric turbulent gravity currents. *J. Fluid Mech.* 308, 289–311.
- Hébert, H., Deplus, C., Huchon, P., Khanbari, K., Audin, L., 2001. Lithospheric structure of a nascent spreading ridge inferred from gravity data: the western Gulf of Aden. *J. Geophys. Res.* 106, 26345–26364.
- Ilıcak, M., Özgökmen, T.M., Peters, H., Baumert, H.Z., Iskandarini, M., 2008. Very large eddy simulation of the red sea overflow. *Ocean Modell.* 20, 183–206.
- Jackett, D.R., McDougall, T.J., 1995. Minimal adjustment of hydrostatic profiles to achieve static stability. *J. Atmos. Oceanic Technol.* 12, 381–389.
- Jungclaus, J.H., Mellor, G., 2000. A three-dimensional model study of the mediterranean outflow. *J. Marine Syst.* 24, 41–66.
- Kantha, L.H., Clayson, C.A., 1994. An improved mixed layer model for geophysical applications. *J. Geophys. Res.* 99, 25235–25266.
- Killworth, P.D., 1977. Mixing on the weddell sea continental slope. *Deep-Sea Res.* 24, 427–448.
- Large, W., Gent, P.R., 1999. Validation of vertical mixing in an equatorial ocean model using large eddy simulations and observations. *J. Phys. Oceanogr.* 29, 449–464.
- Large, W.G., McWilliams, J.C., Doney, S.C., 1994. Oceanic vertical mixing: a review and a model with a nonlocal boundary layer parameterization. *Rev. Geophys.* 32, 363–403.
- Marchesiello, P., McWilliams, J.C., Shchepetkin, A., 2001. Open boundary conditions for long-term integration of regional oceanic models. *Ocean Modell.* 3, 1–20.
- Matt, S., Johns, W.E., 2007. Transport and entrainment in the red sea outflow plume. *J. Phys. Oceanogr.* 37, 819–836.
- Mauritzen, C., Price, J., Sanford, T., Torres, D., 2005. Circulation and mixing in faroese channels. *Deep Sea Res. Part II* 52, 883–913.
- Mellor, G.L., Yamada, T., 1982. Development of a turbulence closure model for geophysical fluid problems. *Rev. Geophys.* 30, 851–875.
- Murray, S.P., Johns, W., 1997. Direct observations of seasonal exchange through the Bab el Mandab Strait. *Geophys. Res. Lett.* 24, 2557–2560.
- Özgökmen, T.M., Chassignet, E., 2002. Dynamics of two-dimensional turbulent bottom gravity currents. *J. Phys. Oceanogr.* 32, 1460–1478.

- Özgökmen, T.M., Fischer, P., 2008. On the role of bottom roughness in overflows. *Ocean Modell.* 20, 336–361.
- Özgökmen, T.M., Johns, W., Peters, H., Matt, S., 2003. Turbulent mixing in the Red Sea outflow plume from a high-resolution nonhydrostatic model. *J. Phys. Oceanogr.* 33.
- Özgökmen, T.M., Fischer, P.F., Duan, J., Iliescu, T., 2004a. Entrainment in bottom gravity currents over complex topography from three-dimensional nonhydrostatic simulations. *Geophys. Res. Lett.* 31, 13212.
- Özgökmen, T.M., Fischer, P.F., Duan, J., Iliescu, T., 2004b. Three-dimensional turbulent bottom density currents from a high-order nonhydrostatic spectral element model. *J. Phys. Oceanogr.* 34.
- Özgökmen, T.M., Fischer, P.F., Johns, W.E., 2006. Product water mass formation by turbulent density currents from a high-order nonhydrostatic spectral element model. *Ocean Modell.* 12, 237–267.
- Peters, H., 1999. Spatial and temporal variability of turbulent mixing in an estuary. *J. Mar. Res.* 57, 805–845.
- Peters, H., Baumert, H.Z., 2007. Validating a turbulence closure against estuarine microstructure measurements. *Ocean Modell.* 19, 183–203.
- Peters, H., Johns, W.E., 2005. Mixing and entrainment in the red sea outflow plume. Part II: turbulence characteristics. *J. Phys. Oceanogr.* 35, 584–600.
- Peters, H., Johns, W.E., ters and Johns, 2006. Bottom layer turbulence in the red sea outflow plume. *J. Phys. Oceanogr.* 36, 1763–1785.
- Peters, H., Baumert, H.Z., Jacob, J.P., 2005a. *Marine Turbulence: Theories, Observations and Models*. Cambridge University Press (Chapter 39).
- Peters, H., Johns, W.E., Bower, A.S., Fratantoni, D.M., 2005b. Mixing and entrainment in the red sea outflow plume. Part I: plume structure. *J. Phys. Oceanogr.* 35, 569–583.
- Polzin, K.L., Toole, J.M., Ledwell, J.R., Schmitt, R.W., 1997. Spatial variability of turbulent mixing in the Abyssal ocean. *Science* 276, 93–96.
- Price, J.F., Baringer, M.O., 1994. Outflows and deep water production by marginal seas. *Prog. Oceanogr.* 33, 161–200.
- Rodi, W., 1980. *Turbulence models and their application in hydraulics*. Tech. rep., Institute of the Association for Hydraulic Research, Delft, The Netherlands.
- Sagaut, P., 2005. *Large Eddy Simulation for Incompressible Flows*, Scientific Computation, an Introduction, third ed. Springer-Verlag, Berlin.
- Schumann, U., Gerz, T., 1995. Turbulent mixing in stably stratified shear flows. *J. Appl. Meteorol.* 34, 33–48.
- Shchepetkin, A.F., McWilliams, J.C., 1998. Quasi-monotone advection schemes based on explicit locally adaptive dissipation. *Mon. Weather Rev.* 126, 1541–1580.
- Shchepetkin, A.F., McWilliams, J.C., 2003. A method for computing horizontal pressure-gradient force in an oceanic model with a nonaligned vertical coordinate. *J. Geophys. Res.* 108, 3090.
- Shchepetkin, A.F., McWilliams, J.C., 2005. The regional oceanic modeling system (roms): a split-explicit, free-surface, topography-following-coordinate oceanic model. *Ocean Modell.* 9, 347–404.
- Simpson, J.E., 1987. *Gravity Currents in the Environment and the Laboratory*. John Wiley and Sons.
- Smith, W.H.F., Sandwell, D.T., 1997. Global seafloor topography from satellite altimetry and ship depth soundings. *Science* 277, 195–196.
- Sofianos, S.S., Johns, W.E., 2001. Wind induced sea level variability in the Red Sea. *Geophys. Res. Lett.* 28, 3175–3178.
- Song, Y., Haidvogel, D., 1994. A semi-implicit ocean circulation model using a generalized topography-following coordinate system. *J. Comput. Phys.* 115, 228–244.
- Turner, J.S., 1986. Turbulent entrainment: the development of the entrainment assumption, and its applications to geophysical flows. *J. Fluid Mech.* 173, 431–471.
- Umlauf, L., Burchard, H., 2003. A generic length-scale equation for geophysical turbulence models. *J. Marine Res.* 61, 235–265.
- Umlauf, L., Burchard, H., 2005. Second-order turbulence closure models for geophysical boundary layers. a review of recent work. *Cont. Shelf Res.* 25, 795–827.
- Umlauf, L., Burchard, H., Hutter, K., 2003. Extending the $k-\omega$ turbulence model towards oceanic applications. *Ocean Modell.* 5, 195–218.
- Warner, J.C., Sherwood, C.R., Arango, H.G., Signell, R.P., 2005. Performance of four turbulence closure methods implemented using a generic length scale method. *Ocean Modell.* 8, 81–113.
- Wesson, J.C., Gregg, M.C., 1994. Mixing at Camarinal Sill in the Strait of Gibraltar. *J. Geophys. Res.* 99, 9847–9878.
- Wu, W., Danabasoglu, G., Large, W.G., 2007. On the effects of parameterized Mediterranean overflow on North Atlantic ocean circulation and climate. *Ocean Modell.* 19, 31–52.
- Xu, X., Chang, Y.S., Peters, H., Özgökmen, T.M., Chassignet, E.P., 2006. Parameterization of gravity current entrainment for ocean circulation models using a high-order 3d nonhydrostatic spectral element model. *Ocean Modell.* 14, 19–44.